Modal contributions and effects of spurious poles in nonlinear subspace identification

Modal contributions and effects of spurious poles in nonlinear subspace identification

S. Marchesiello, A. Fasana and L. Garibaldi

Department of Mechanical and Aerospace Engineering, Politecnico di Torino, Corso Duca degli Abruzzi 24, 10129 Torino, Italy.

https://doi.org/10.1016/j.ymssp.2015.05.008

Cite as:

S. Marchesiello, A. Fasana, L. Garibaldi, Modal contributions and effects of spurious poles in nonlinear subspace identification. MECHANICAL SYSTEMS AND SIGNAL PROCESSING, vol. 74, p. 111-132, ISSN: 0888-3270, doi: 10.1016/j.ymssp.2015.05.008

Modal contributions and effects of spurious poles in nonlinear subspace identification

S. Marchesiello*, A. Fasana and L. Garibaldi

Dipartimento di Ingegneria Meccanica e Aerospaziale

Politecnico di Torino

Corso Duca degli Abruzzi 24, 10129 Torino, Italy

Abstract

Stabilisation diagrams have become a standard tool in the linear system identification, due to the capability of reducing the user interaction during the parameter extraction process. Their use in the presence of nonlinearity was recently introduced and it was demonstrated to be effective even in presence of non-smooth nonlinearities and high modal density. However, some variability of the identification results was reported, in particular concerning the quantification of the nonlinear effects, because of the presence of spurious modes, due to an over-estimation of the system order.

In this paper the impact of spurious poles on the nonlinear subspace identification is investigated and some modal decoupling tools are introduced, which make it possible to identify modal contributions of physical poles on the nonlinear dynamics. An

* Corresponding author. Tel.: +390110906947: fax: +390110906999; e-mail address:

experimental identification is then conducted on a multi-degree-of-freedom system with a local nonlinearity and the significant improvements of the estimates obtained by the proposed approach are highlighted.

Keywords: nonlinear identification; stabilisation diagrams; modal mass; subspace methods.

1. Introduction

It is well known that conventional linear estimators give contaminated results in presence of nonlinearities and the extraction of the underlying linear system properties hence becomes a difficult task. To solve this problem, in the last three decades several nonlinear identification methods have been developed, most of them being applicable to single-degree-of-freedom (SDOF) systems. More recently, multi-degree-of-freedom (MDOF) systems have been successfully dealt with [1]; however, only a limited number of nonlinear terms and degrees of freedom were included, due to the complexity of algorithms and required computational effort. To overcome these problems, the method called nonlinear subspace identification (NSI) has been proposed [2], by using the perspective of nonlinearities as unmeasured internal feedback forces [3]. This time domain method exploits the robustness and high numerical performances of algorithms, i.e., the basis of the stochastic subspace identification (SSI), successfully adopted in many linear applications [4-10]. A dual approach has been developed in the frequency domain, termed frequency-domain nonlinear subspace identification (FNSI) method [11], which allows to discriminate frequencies according to information content and signal-to-noise ratio (SNR), thus increasing the accuracy and reducing the

stefano.marchesiello@polito.it

computational burden.

It is a matter of fact that system identification results are improved by over-specifying the model order [6], computing system poles and then removing spurious poles. This is usually performed with the help of stabilisation diagrams, constructed by estimating poles with increasing model order and by plotting only those poles for which the relative difference in modal frequency, damping ratio and shape is below a user-defined value. In order to make stabilisation diagrams clearer, the modal transfer norm was proposed in [7] for a combined deterministic-stochastic subspace identification. Moreover, different techniques were introduced to reduce the user interaction: a clustering algorithm was proposed in [12], a component energy index was defined in [9] to estimate the model order and a hierarchical clustering algorithm was adopted in [10] for analyzing continuously collected data of a bridge.

The use of stabilisation diagrams in the presence of nonlinearity was first introduced in [13] and it was demonstrated to be effective for retrieving linear system parameters from nonlinear data generated by numerical experiments, even in presence of non-smooth nonlinearities, high modal density and high non-proportional damping. However, some variability of the identification results was reported, in particular concerning the quantification of the nonlinear effects.

The objective of the present paper is to investigate the role of spurious poles, to show how they affect the estimates of the nonlinear contributions to the system dynamics and how to improve the estimates. For this investigation, a modal decoupling procedure is introduced and the modal mass is computed for system poles. This procedure is illustrated by processing experimental measurements conducted on a scaled building connected to a metallic wire, which adds strong nonlinear effects. A new perspective is finally introduced, based on the identification of modal contributions due to physical

poles on the nonlinear dynamics.

The paper is organised as follows. The theoretical background of the NSI is outlined in Section 2. This is followed by the description of modal decoupling tools (Section 3), which act in conjunction with stabilisation diagrams to remove spurious poles. A numerical validation is conducted in Section 4, where a system of low dimensions is studied. The experimental work is finally described in Section 5, where the parameter estimation is conducted both with low excitation level (linear identification) and high excitation level (nonlinear identification). The conclusions of the present study are summarised in Section 6.

2. Nonlinear subspace identification

Let us consider the equation of motion of a dynamical discrete system with *h* degrees of freedom, carrying lumped nonlinear springs and dampers:

$$\mathbf{M}\ddot{\mathbf{z}}(t)+\mathbf{C}_v\dot{\mathbf{z}}(t)+\mathbf{K}\mathbf{z}(t)+\sum_{j=1}^{p}\mu_j\mathbf{L}_{nj}g_j(t)=\mathbf{f}(t) \tag{1}$$

where $\mathbf{M}$, $\mathbf{C}_v$ and $\mathbf{K}$ are the mass, viscous damping and stiffness matrices respectively, $\mathbf{z}(t)$ is the generalised displacement vector and $\mathbf{f}(t)$ the generalised force vector, both of dimension *h*, at time *t*. The nonlinear term $\mathbf{N}[\mathbf{z}(t),\dot{\mathbf{z}}(t)]=\sum_{j=1}^{p}\mu_j\mathbf{L}_{nj}g_j(t)$ is expressed as the sum of *p* components, each of them depending on the scalar nonlinear function $g_j(t)$, which indicates the class of the nonlinearity, through a location vector $\mathbf{L}_{nj}$, whose elements may assume the values 1, -1 or 0. By moving the nonlinear terms of Eq. (1) to the right hand side

$$\mathbf{M}\ddot{\mathbf{z}}(t)+\mathbf{C}_v\dot{\mathbf{z}}(t)+\mathbf{K}\mathbf{z}(t)=\mathbf{f}(t)-\sum_{j=1}^{p}\mu_j\mathbf{L}_{nj}g_j(t)=\mathbf{f}(t)-\mathbf{f}_{nl}(t) \tag{2}$$

the original system may be viewed as subjected to the external forces $\mathbf{f}(t)$ and the internal feedback forces caused by nonlinearities $\mathbf{f}_{nl}(t)$. This perspective, already chosen in [3] to develop the frequency domain method called nonlinear identification through feedback of the outputs (NIFO), is on the basis of the present time domain identification method, referred to as NSI [2]. In the case of measurements **y** involving displacements only, the state-space formulation of the equation of motion is

$$\begin{Bmatrix}\dot{\mathbf{z}}\\ \ddot{\mathbf{z}}\end{Bmatrix}=\begin{bmatrix}\mathbf{0}_{h\times h} & \mathbf{I}_{h\times h}\\ -\mathbf{M}^{-1}\mathbf{K} & -\mathbf{M}^{-1}\mathbf{C}_v\end{bmatrix}\begin{Bmatrix}\mathbf{z}\\ \dot{\mathbf{z}}\end{Bmatrix}+\begin{bmatrix}\mathbf{0}_{h\times h} & \mathbf{0}_{h\times 1} & \cdots & \mathbf{0}_{h\times 1}\\ \mathbf{M}^{-1} & \mathbf{M}^{-1}\mu_1\mathbf{L}_{n1}\cdots & \mathbf{M}^{-1}\mu_p\mathbf{L}_{np}\end{bmatrix}\begin{bmatrix}\mathbf{f}(t)^T & -g_1(t) & \cdots & -g_p(t)\end{bmatrix}^T \tag{3}$$

$$\mathbf{y}=\begin{bmatrix}\mathbf{I}_{h\times h} & \mathbf{0}_{h\times h}\end{bmatrix}\begin{Bmatrix}\mathbf{z}\\ \dot{\mathbf{z}}\end{Bmatrix}+\begin{bmatrix}\mathbf{0}_{h\times h} & \mathbf{0}_{h\times 1} & \cdots & \mathbf{0}_{h\times 1}\end{bmatrix}\begin{bmatrix}\mathbf{f}(t)^T & -g_1(t) & \cdots & -g_p(t)\end{bmatrix}^T \tag{4}$$

corresponding to the state vector $\mathbf{x}=\begin{bmatrix}\mathbf{z}^{\mathrm{T}} & \dot{\mathbf{z}}^{\mathrm{T}}\end{bmatrix}^{\mathrm{T}}$ (superscript T denotes transposition) and to the input vector $\mathbf{u}=\begin{bmatrix}\mathbf{f}(t)^T & -g_1(t) & \cdots & -g_p(t)\end{bmatrix}^T$ or, in a more compact form

$$\begin{aligned}\dot{\mathbf{x}}&=\mathbf{A}_c\mathbf{x}+\mathbf{B}_c\mathbf{u}\\ \mathbf{y}&=\mathbf{C}\mathbf{x}\ +\mathbf{D}\mathbf{u}\end{aligned} \tag{5}$$

This continuous model may be converted into the following discrete state-space model, assuming zero-order hold for the input $\mathbf{u}$ with sampling period Δt:

$$\begin{aligned}\mathbf{x}_{k+1}&=\mathbf{A}\mathbf{x}_k+\mathbf{B}\mathbf{u}_k\\ \mathbf{y}_k&=\mathbf{C}\mathbf{x}_k\ +\mathbf{D}\mathbf{u}_k\end{aligned} \tag{6}$$

where

$$\mathbf{A}=\mathrm{e}^{\mathbf{A}_c\Delta t} \tag{7}$$

is the dynamical system matrix,

$$\mathbf{B} = \left(\mathrm{e}^{\mathbf{A}_c \Delta t} - \mathbf{I}_{2h\times 2h}\right)\mathbf{A}_c^{-1}\mathbf{B}_c \tag{8}$$

is the input matrix, which represents the linear transformation by which the inputs influence the next state, **C** is the output matrix, that describes how the internal state is transferred to the measurements $\mathbf{y}_k$, and **D** is the direct feedthrough matrix.

The nonlinear subspace identification procedure is based on the estimation of the state space matrices **A**, **B**, **C** and **D** obtained within a similarity transformation, by a subspace method in the time domain [4], and on the subsequent computation of system parameters from the matrix

$$\mathbf{H}_E(\omega) = \mathbf{D} + \mathbf{C}\left(z\mathbf{I}_{2h\times 2h} - \mathbf{A}\right)^{-1}\mathbf{B}, \quad z = e^{\mathrm{i}\omega\Delta \mathrm{t}} \tag{9}$$

here defined "extended" frequency response function (FRF) matrix, because it also includes nonlinear terms in the multiple input multiple output (MIMO) model. From this matrix, which is invariant under the similarity transformation, system parameters (and in particular μ_j) may be extracted, making it possible to predict the nonlinear system response to a measured input. After some mathematical manipulations [2] it can be proven that:

$$\mathbf{H}_E(\omega) = \left[\mathbf{H} \quad \mathbf{H}\mu_1\mathbf{L}_{n1} \quad \ldots \quad \mathbf{H}\mu_p\mathbf{L}_{np}\right] \tag{10}$$

where

$$\mathbf{H}(\omega) = \left(\mathbf{K} + \mathrm{i}\omega\mathbf{C}_v - \omega^2\mathbf{M}\right)^{-1} \tag{11}$$

is the underlying linear system receptance matrix. Similar steps are needed in the case where accelerations are measured [14]. The nonlinear coefficients identified from $\mathbf{H}_E(\omega)$ are complex-valued and frequency-dependent. However, in the absence of modelling errors and noise and by assuming an infinite number of available data, the

real parts of the coefficients converge to their exact values with no frequency dependence, and the imaginary parts converge to zero. An appropriate selection of the nonlinear functional forms $g_j(t)$ should therefore make the imaginary parts much smaller than the corresponding real parts and the frequency dependence of the coefficients should also remain small [13].

3. Stabilisation diagrams and modal contributions

Subspace methods take advantage of robust numerical techniques such as QR factorisation and singular value decomposition (SVD) by using geometric tools such as the oblique projections of the row space of matrices. These methods have been successfully adopted in many experimental cases [5-10]. For a complete description of the estimating procedure see [4].

A crucial step of the stochastic subspace identification, as of many other identification methods, is the selection of the appropriate model order to capture the modes present in the frequency range of interest. In numerical examples concerning discrete vibrating systems [2] this model order can be selected by inspecting the singular value plot, since a jump of many orders of magnitude may be observed, in particular when the SNR is high. However, for real structures this criterion usually cannot be applied because no jump is evident in the singular value plot. Moreover, in order to obtain accurate estimates of the modal parameters an over-specification of the model order is needed, because of the presence of noise in the data, but this results in a number of spurious numerical modes. Models of increasing order are determined by rejecting fewer singular values, thus producing a set of modal parameters, which can be plotted in a stabilisation diagram.

As pointed out in [8], there are many origins of uncertainty on the identified system

parameters, including the limited number of data samples, non-stationary effects (e.g. moving masses), analogue or digital filtering, measurement noise and nonlinear modelling errors that result in spurious poles. Part of the bias error may be removed by using stabilisation diagrams and, for this reason, they have become one of the most widely used tools to detect physical poles and extract modal parameters afterwards. System modal parameters can be computed starting from the eigenvalue decomposition:

$$\mathbf{A} = \mathbf{\Psi \Lambda \Psi}^{-1} \tag{12}$$

where $\mathbf{A}$ is the discrete-time state matrix, related with its continuous-time counterpart by $\mathbf{A} = \mathrm{e}^{\mathbf{A}_c \Delta t}$; $\mathbf{\Lambda}$ is the diagonal matrix of discrete eigenvalues (λ_1,..., λ_n). These can be transformed into continuous eigenvalues λ_{ci} of the mechanical system as follows

$$\lambda_{ci} = \frac{1}{\Delta t} \ln(\lambda_i) \tag{13}$$

The natural frequency and modal damping ratio are calculated as

$$f_i = \frac{|\lambda_{ci}|}{2\pi} \quad \text{and} \quad \zeta_i = \frac{-\mathrm{Re}(\lambda_{ci})}{|\lambda_{ci}|} \tag{14}$$

while the mode shapes ϕ_i evaluated at the sensor locations are the columns of $\mathbf{\Phi}$, which is given by

$$\mathbf{\Phi} = \mathbf{C\Psi} \tag{15}$$

In order to select the physical modes, stabilisation diagrams for both eigenfrequencies and damping ratios are needed; stabilisation between two consecutive extracted mode shapes, is also evaluated by computing, for instance, the modal assurance criterion:

$$MAC_{i,j} = \frac{\left|\phi_i^H \phi_j\right|}{\left(\phi_i^H \phi_i\right)\left(\phi_j^H \phi_j\right)} \tag{16}$$

where the superscript H denotes the complex transposed.

As shown in [5] in case of close eigenfrequencies, a peculiar strategy has to be adopted to split the modes. As the model order increases, the extracted mode shapes are compared with those of the previous step by means of the MAC: the mode shape giving the higher MAC is accepted.

Generally only those poles, for which the relative difference in eigenfrequency and damping ratio is below a user defined threshold value, and also showing a sufficiently high MAC, are plotted in the stabilisation diagram: this is often sufficient to eliminate spurious modes with no physical meaning. Other indicators such as very high damping ratio, complex and/or unrealistic mode shape may help to remove spurious poles.

One of the advantages of the state-space description is that the contributions of different modes to the system FRFs can be easily decoupled. As will be demonstrated in the experimental application, this property is fundamental to remove the contributions of spurious poles, which can dramatically affect the estimates of the nonlinear coefficients μ_j.

To this purpose, the state-space model (6) can be rewritten by exploiting a similarity transform of the system matrix $\mathbf{A}$ [7]

$$\begin{aligned} \mathbf{x}_{k+1}^m &= \mathbf{\Lambda}\mathbf{x}_k^m + \mathbf{B}^m\mathbf{u}_k \\ \mathbf{y}_k &= \mathbf{C}^m\mathbf{x}_k^m + \mathbf{D}\mathbf{u}_k \end{aligned} \tag{17}$$

where $\mathbf{A} = \mathbf{\Psi}\mathbf{\Lambda}\mathbf{\Psi}^{-1}$ is the spectral decomposition of $\mathbf{A}$, Eq. (12), $\mathbf{x}_k^m = \mathbf{\Psi}^{-1}\mathbf{x}_k$, $\mathbf{B}^m = \mathbf{\Psi}^{-1}\mathbf{B}$ and $\mathbf{C}^m = \mathbf{C}\mathbf{\Psi}$. Since the eigenvalue matrix $\mathbf{\Lambda}$ is diagonal, a new expression of the extended FRF matrix can be written if the measured outputs are displacements or velocities $(\mathbf{D} = \mathbf{0})$:

$$\mathbf{H}_E(\omega) = \mathbf{C}^m\left(z\mathbf{I}\text{-}\mathbf{\Lambda}\right)^{-1}\mathbf{B}^m = \sum_{i=1}^{n}\frac{\mathbf{c}_i^m\mathbf{b}_i^m}{z-\lambda_i}, \quad z = e^{\mathrm{i}\omega\Delta\mathrm{t}} \tag{18}$$

where $\mathbf{c}_i^m$ is the *i*th column of $\mathbf{C}^m$ and $\mathbf{b}_i^m$ the *i*th row of $\mathbf{B}^m$. If only accelerations are measured the FRF can be decoupled as:

$$\mathbf{H}_E(\omega) = \mathbf{D}^m + \mathbf{C}^m(z\mathbf{I}\text{-}\boldsymbol{\Lambda})^{-1}\mathbf{B}^m = \sum_{i=1}^{n} \frac{(z-1)\mathbf{c}_i^m \mathbf{b}_i^m}{(\lambda_i - 1)(z-\lambda_i)}, \quad z = e^{\mathrm{i}\omega\Delta\mathrm{t}} \tag{19}$$

Both expressions were originally derived for linear systems ($p = 0$) [7]. In order to introduce the modal contributions let's consider a scalar (linear) FRF corresponding to the input *q* and response *p* degrees of freedom, in case of underdamped modes:

$$H_{pq}(\omega) = \sum_{r=1}^{n/2} \left(\frac{A_{pqr}}{\mathrm{i}\omega - \lambda_{cr}} + \frac{A_{pqr}^*}{\mathrm{i}\omega - \lambda_{cr}^*} \right) \tag{20}$$

where $A_{pqr} = Q_r \phi_{pr} \phi_{qr}$ is the residue of the *r*th mode, Q_r is the modal scaling, ϕ_{pr} and ϕ_{qr} are modal coefficients, superscript * denotes complex conjugate. The driving-point residue, $A_{qqr} = Q_r \phi_{qr}^2$ is used to derive the modal scaling. For proportionally damped systems, the *r*th modal mass can be defined as [15]:

$$M_r = \frac{1}{2\mathrm{i}Q_r \omega_{dr}} \tag{21}$$

ω_{dr} being the damped natural frequency of the *r*th mode. Let's consider a vibrating system consisting of *N* masses with no rotational motion (as in the experimental case, Section 5). If the largest scaled modal coefficient is equal to unity, the modal mass computed according to Eq. (21) will be a number between zero and the total mass of the system. Indeed the *r*th modal mass can be computed as:

$$M_r = \begin{bmatrix} \phi_{1r} & \phi_{2r} & \cdots & \phi_{Nr} \end{bmatrix} \begin{bmatrix} m_1 & 0 & \cdots & 0 \\ 0 & m_2 & & \vdots \\ \vdots & & \ddots & 0 \\ 0 & \cdots & 0 & m_N \end{bmatrix} \begin{bmatrix} \phi_{1r} \\ \phi_{2r} \\ \vdots \\ \phi_{Nr} \end{bmatrix} = \sum_{j=1}^{N} m_j \phi_{jr}^2 \le \sum_{j=1}^{N} m_j \tag{22}$$

because $\phi_{jr}^2 \leq 1$. By applying this modal vector scaling (or a different one), the modal mass can be used as an extra criterion in stabilisation diagrams, as supposed in [7]. If measurements are performed in terms of velocity over force or acceleration over force, Eq. (21) will have to be altered accordingly.

First the residues and then the modal masses are obtained considering that the modal decomposition, Eq. (18) (discrete-time parameters) and Eq. (20) (continuous-time parameters) should match [7] for each element H_{pq} of the underlying linear system FRF matrix $\mathbf{H}$. In the same manner it is possible to compute the modal mass when accelerations are measured, starting from the receptance (20) weighted by $-\omega^2$.

Table 1

Numerical example parameters

Mass (kg)	Linear stiffness (N/m)	Damping (Ns/m)	Nonlinear stiffness (N/m^3)
$m_1 = 25$; $m_2 = 18$;	$k_1 = 3\times10^4$;	$c_1 = c_2 = c_3 = 10$;	
$m_3 = 15$; $m_4 = 25$	$k_2 = k_3 = k_4 = 5\times10^4$;	$c_4 = c_5 = c_6 = c_7 = 10$;	$k_{nl} = 5\times10^{10}$
	$k_5 = k_6 = k_7 = 5\times10^4$		

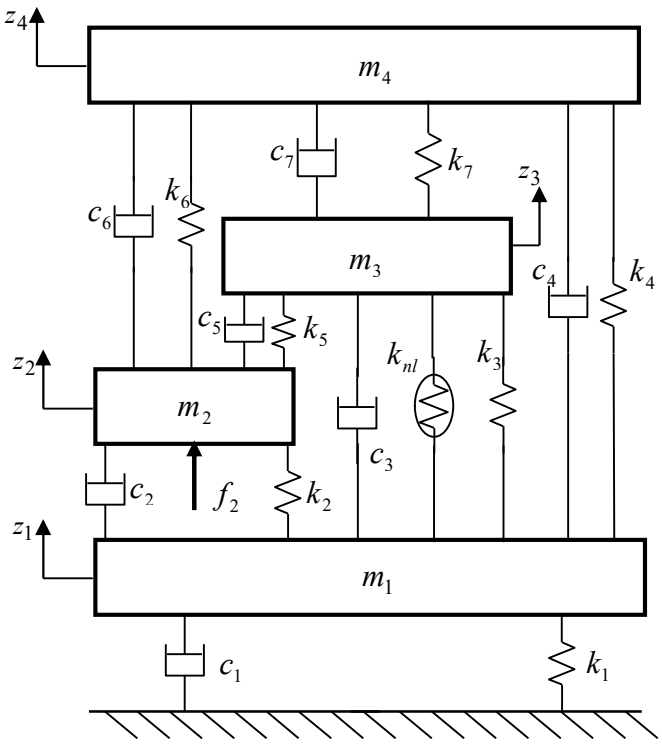

Figure 1: 4-DOF nonlinear system with a cubic stiffness located between DOF 1 and 3.

4. Numerical application

A numerical example with a single cubic nonlinear stiffness is considered hereafter to validate the procedure discussed in the previous section. The four-degree-of-freedom nonlinear system shown in Fig. 1 is excited at DOF 2 only; a nonlinear term is included in the equation of motion (1):

$$\mu_1 \mathbf{L}_{n1} g_1(t) = k_{nl} \begin{bmatrix} -1 & 0 & 1 & 0 \end{bmatrix}^T (z_3 - z_1)^3 \tag{23}$$

with system parameters summarised in Table 1. In this case the extended FRF matrix is

$$\mathbf{H}_E(\omega) = \begin{bmatrix} \mathbf{H} & \mathbf{H}\mu_1 \mathbf{L}_{n1} \end{bmatrix} \tag{24}$$

where **H** is the FRF matrix of the underlying linear system. Since the force is applied at DOF 2, only the second column of this matrix can be estimated. However, the reciprocity relationships $H_{21} = H_{12}$, $H_{23} = H_{32}$ and $H_{24} = H_{42}$ (which hold true because **H** is related to a linear system) can be applied, and this is sufficient to compute μ_1 from the second element of the following vector (the symbol ? denotes unknown terms)

$$\mathbf{H}\mu_1 \mathbf{L}_{n1} = \mu_1 \begin{bmatrix} ? & H_{12} & ? & ? \\ H_{21} & H_{22} & H_{23} & H_{24} \\ ? & H_{32} & ? & ? \\ ? & H_{42} & ? & ? \end{bmatrix} \begin{Bmatrix} -1 \\ 0 \\ 1 \\ 0 \end{Bmatrix} = \mu_1 \begin{Bmatrix} ? \\ H_{23} - H_{21} \\ ? \\ ? \end{Bmatrix} \tag{25}$$

The estimate of the nonlinear term coefficient is given by:

$$k_{nl} = \frac{H_{E22}(\omega)}{H_{E31}(\omega) - H_{E11}(\omega)} = \frac{H_{E22}(\omega)}{H_{23}(\omega) - H_{21}(\omega)} = \frac{\sum_{r=1}^{n/2} num_r(\omega)}{\sum_{r=1}^{n/2} den_r(\omega)} \tag{26}$$

It is important to recall that both numerator and denominator can be expressed as a sum of "modal contributions", computed by using Eq. (19). Each of them is given by two

terms, built by complex conjugate elements in presence of underdamped modes only (see also Eq. 20). However, this makes it difficult to give an appropriate definition for the actual contribution of each mode to the coefficient k_{nl}, which appears as a complex function of the real variable ω, in the form of ratio of two sums.

In a first simulation, the exact matrices built on the system parameters (Table 1) have been used to construct the extended FRF matrix: obviously, the exact model order $n = 8$ is chosen and no error is found. The coefficient of the cubic nonlinearity as it is "seen" by each of the four physical modes can be defined as follows:

$$k_{nl}^{r}(\omega) = \frac{num_r(\omega)}{den_r(\omega)}, \quad r = 1, 2, 3, 4 \tag{27}$$

These coefficients are depicted in Fig. 2, which is very useful to demonstrate that, a well identified physical mode can be used to obtain information about the nonlinearity. The figure also shows that, in the case of perfect identification, no frequency dependence of the nonlinear coefficient is expected.

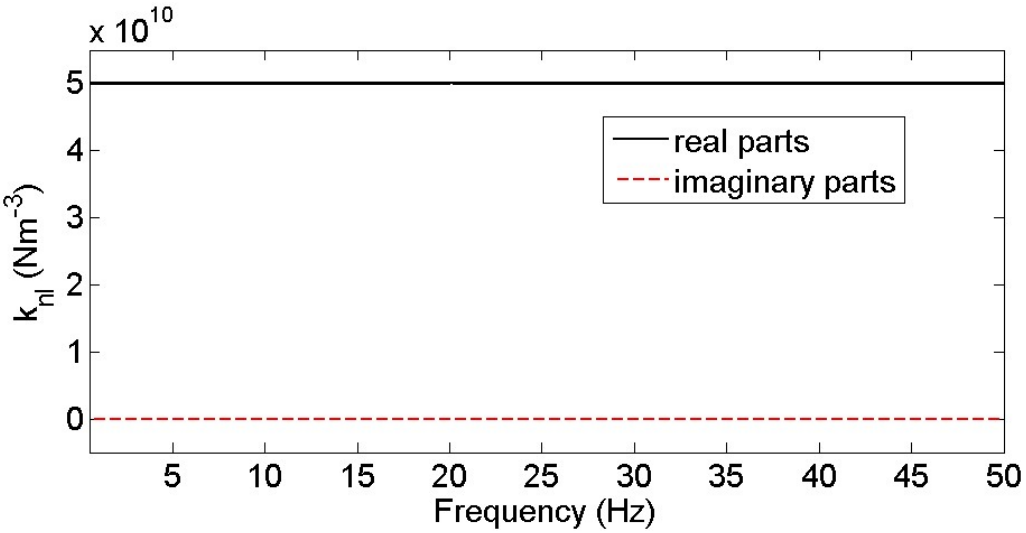

Figure 2: Numerical example with exact matrices. Real and imaginary parts of the coefficient k_{nl}^{r} as computed by the contribution of the rth mode only (model order $n = 8$). The curves for the four modes are superimposed.

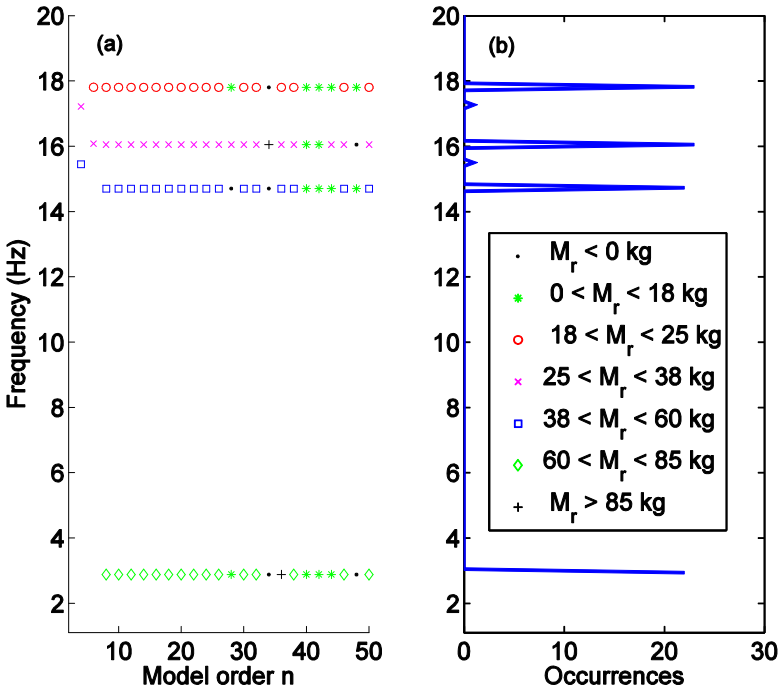

Figure 3: Eigenfrequencies of the underlying linear system for the numerical example, extracted by NSI with increasing model orders (a); histogram of the frequency occurrences (b). The modal mass associated to each pole is indicated by different markers.

Afterwards, the system is excited by a zero-mean Gaussian random force (with r.m.s. = 50 N), time histories are obtained by a Runge-Kutta numerical integration and 1% of zero-mean Gaussian noise is added to each simulated acceleration, with sampling frequency of 4 kHz and duration of 80 s. The eigenfrequencies of the underlying linear system extracted by NSI with increasing model orders (from 2 to 50, even values only) are shown in Fig. 3 together with the associated modal masses. The modal mass is computed by imposing the largest scaled modal coefficient equal to unity: as discussed in Section 3, with this scaling criterion the modal mass has a physical significance, being always less than the total mass of the system. In the frequency range between 0 and 18 Hz, spurious poles are not present, while they appears at higher frequencies (the situation is more complicated in experimental cases, as shown later).

The present test case shows that poles with frequency higher than 18 Hz (definitely spurious ones) are associated with modal masses which are negative or higher than the total mass of the system (83 kg) in 98% of the cases. In fact, the modal masses of spurious poles are usually negative or higher than those of physical poles (differences are often of several orders of magnitude): however, a theoretical evidence to support this particular property is hard to be given.

In classical stabilisation diagrams (Fig. 4) system poles are defined as "stable" if by increasing the model order the relative difference in modal frequency, damping ratio and shape is below a user-defined value. However, these diagrams give partial information

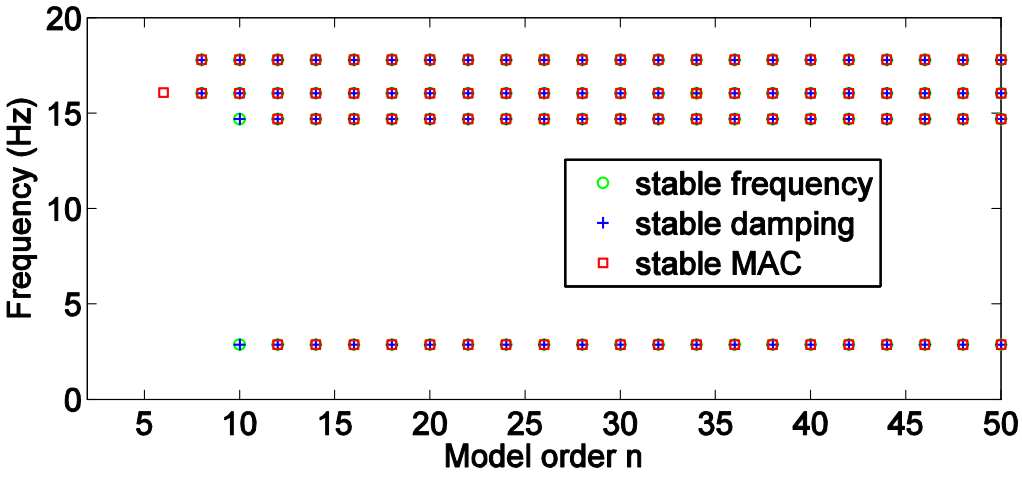

Figure 4: Stabilisation diagram computed by NSI for the numerical example. Stabilisation thresholds for natural frequency, damping ratio and MAC are 0.5 %, 5 % and 0.98, respectively.

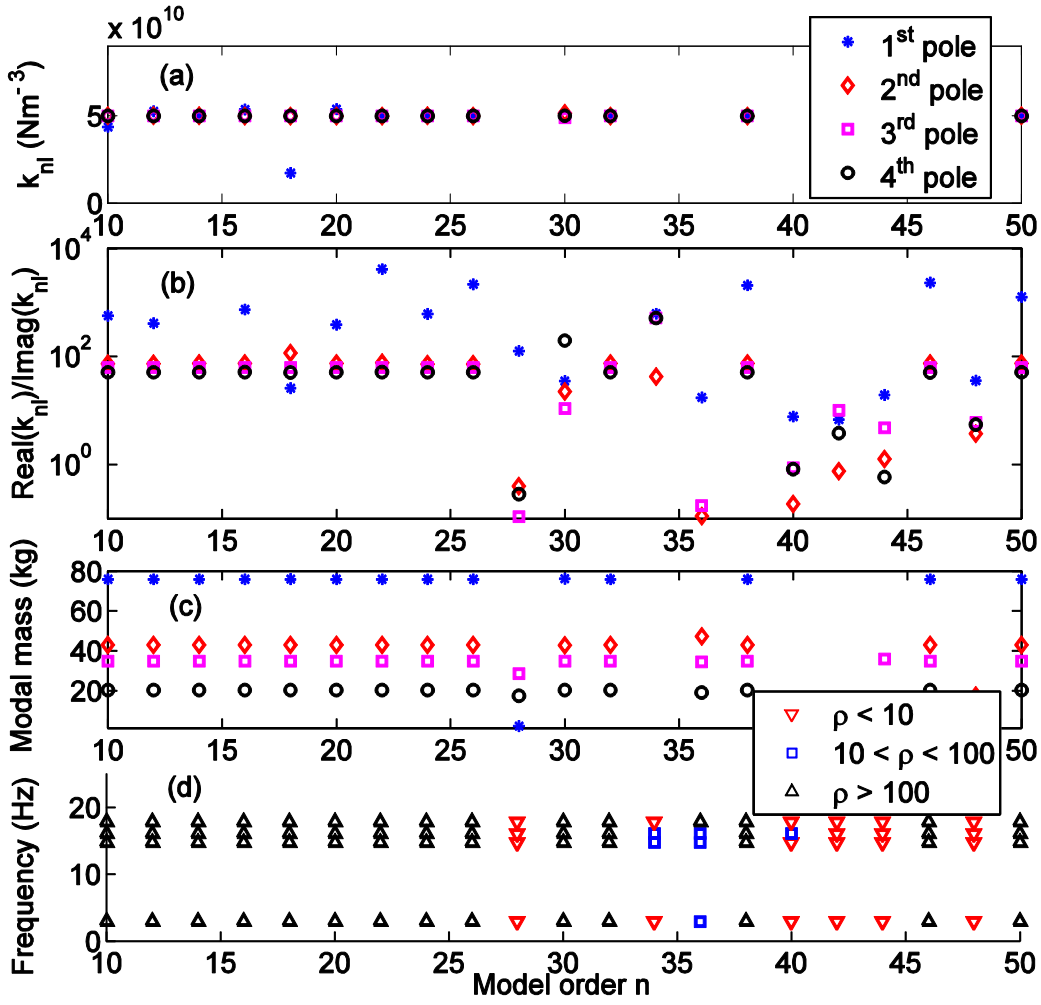

Figure 5: Stabilisation diagrams computed by NSI for the numerical example. (a) real part; (b) ratio between the real and the imaginary parts of the spectral mean for the single-mode coefficient k_{nl}^r; (c) modal masses of the four physical poles (each pole is indicated by a different marker); (d) ratio ρ between the real and the imaginary parts of the modal mass associated to each pole.

about the identification of the underlying linear system FRFs and about the nonlinear coefficients. For this reason, more powerful stabilisation diagrams are proposed as shown in Fig 5: figures 5a and 5b show the real part and the ratio between the real and the imaginary parts of the spectral mean (from 1 Hz to 50 Hz) for the single-mode coefficient k_{nl}^r; figures 5c and 5d show the modal mass M_r associated to each pole and the corresponding ratio $\rho = \frac{real(M_r)}{imag(M_r)}$. These diagrams can be used to select the model order properly: they indicate

that for some model orders results are not reliable, because the imaginary part of the nonlinear coefficient is too high (Fig. 5b) and because the imaginary part of the modal mass is too high (Fig. 5d). Actually, the last criterion only holds when the linear damping distribution is proportional to the mass and stiffness distributions. This assumption (real modes and real-valued modal mass) is compatible with the presence of weak damping as in the present case (the maximum damping ratio is 1.1%). In the general case of nonproportional damping the "modal A" and "modal B" should be used instead [15].

Note that using classical stabilisation diagrams in the nonlinear identification could be misleading: from Fig. 4 four "stable" poles are identified after $n = 12$, but for example the nonlinear coefficient for the model order $n = 28$ is completely wrong (the minimum error is obtained from the fourth pole as $k_{nl}^4 = 7.5\times10^{11} - \mathrm{i}2.2\times10^{12}$ N/m^3, which is out of the scale of Fig. 5a). In fact, with the use of Figures 5b-c-d, this pole would be discarded. A good choice could be $n = 22$ and in this case the underlying linear system FRFs are synthesised by using the modal decomposition (Eq. 19): the FRF shown in Fig. 6 is in excellent agreement with the theoretical solution (errors are four orders of magnitude smaller than the true values). Finally, Fig. 7 shows the single-mode nonlinear coefficients k_{nl}^r: the frequency dependence is minimum and the imaginary part is very small, which confirms the quality of the identification. More precisely, the maximum error of the spectral mean is 0.26% for the real part estimated by the first mode, while the maximum imaginary part is 1.9% of the true k_{nl} value for the contribution of the fourth mode.

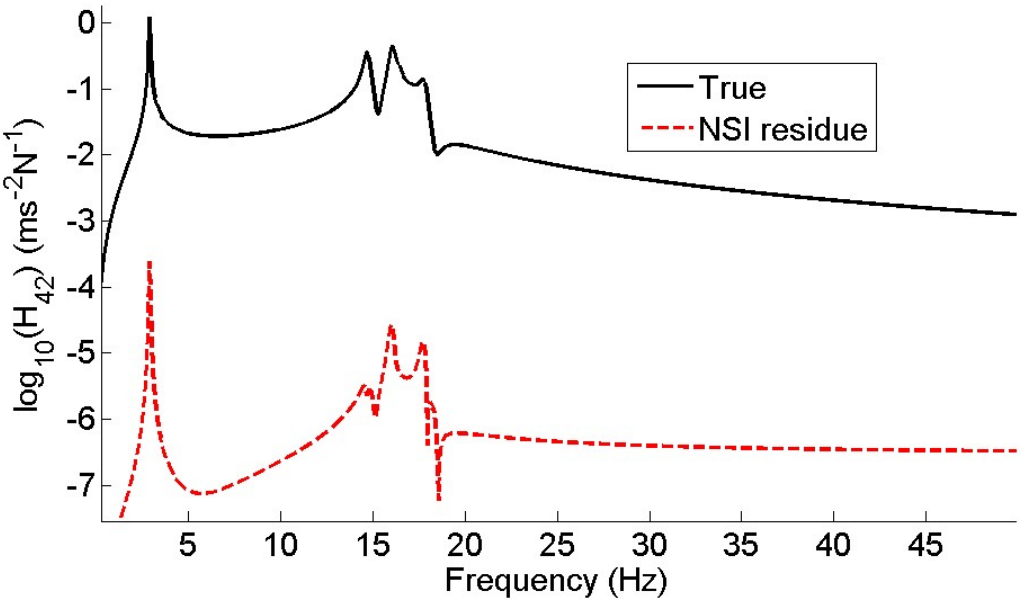

Figure 6: Magnitude of the true H_{42} (solid line), four-modes synthesis residue of the underlying linear system FRF estimated by NSI with model order $n = 22$ (dashed line). The residue has been computed as $\left|\text{estimated} - \text{actual}\right|$.

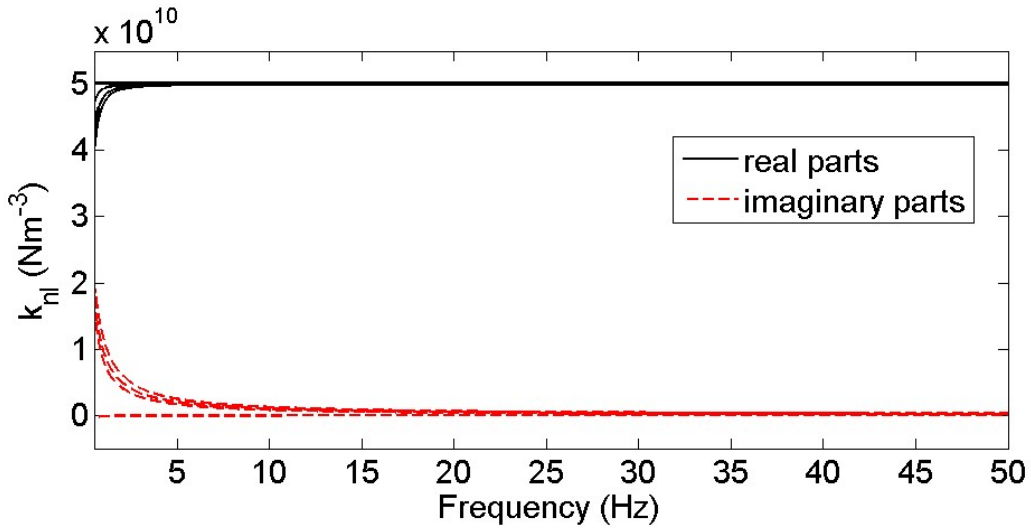

Figure 7: Real and imaginary parts of the four coefficients k_{nl}^{r} as computed by the contribution of the rth mode only (model order $n = 22$).

5. Experimental application

The investigated structure is constructed with aluminium decks linked by thin steel

beams (see Fig. 8), whose properties are summarised in Table 2. The rig may be reasonably considered as a 5 DOFs vibrating system, because the plate stiffness is considerable and each horizontal displacement z_i is only associated to the flexural stiffness of the vertical beams. The structure shown in Fig. 9a is excited by means of an electrodynamic shaker acting on the second floor. A thin metallic wire with small pretension is connected to the fifth floor (Fig. 9b), whose amplitude of motion, if high enough, makes the restoring force nonlinear. It is assumed that the force produced by the wire has the form $f_{nl} = k_l z_5 + k_{nl} z_5^3$, which corresponds to the Taylor-series expansion to the third order of the restoring force, with a good degree of approximation in practical cases [16].

The acceleration of each floor and the force applied by the shaker were measured with different levels of band-limited noise between 0.5 and 40 Hz, with sampling frequency of 409.6 Hz and duration of 300 s (122880 samples per channel). An estimate of the fifth floor displacement was obtained by integrating twice the corresponding acceleration and then by filtering the resulting signal (between 2 and 160 Hz) to remove the spurious components introduced by the integration procedure. The displacement of the fifth floor when the system is excited by a linear sine sweep between 3 and 7 Hz in 300 s (Fig.10) clearly indicates a jump phenomenon, which highlights the nonlinear behaviour [17].

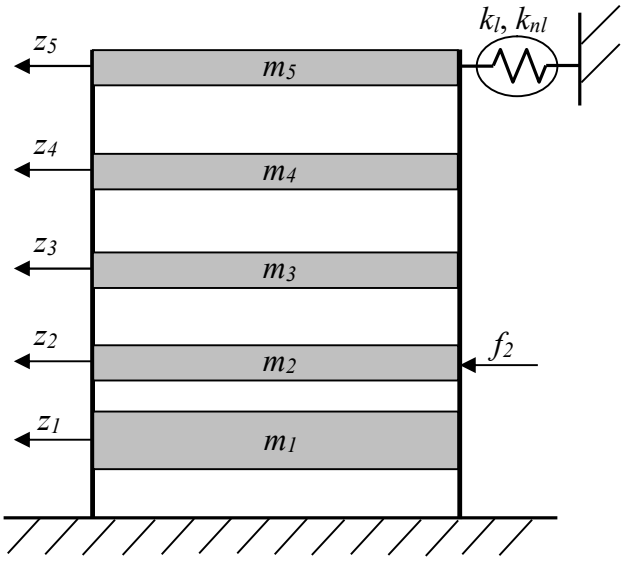

Figure 8: Multi-storey building with nonlinearity produced by a thin wire.

Table 2

Structure characteristics

element	plate				vertical beam	
i	mass (kg)	width (mm)	length (mm)	thickness (mm)	length (mm)	cross sectional area (mm^2)
1	4.32	270	250	24	50	60×0.3
2	2.14	270	250	12	30	60×0.3
3	1.89	270	250	10	60	60×0.3
4	1.82	270	250	10	60	60×0.3
5	1.95	270	250	10	60	60×0.3

(a)

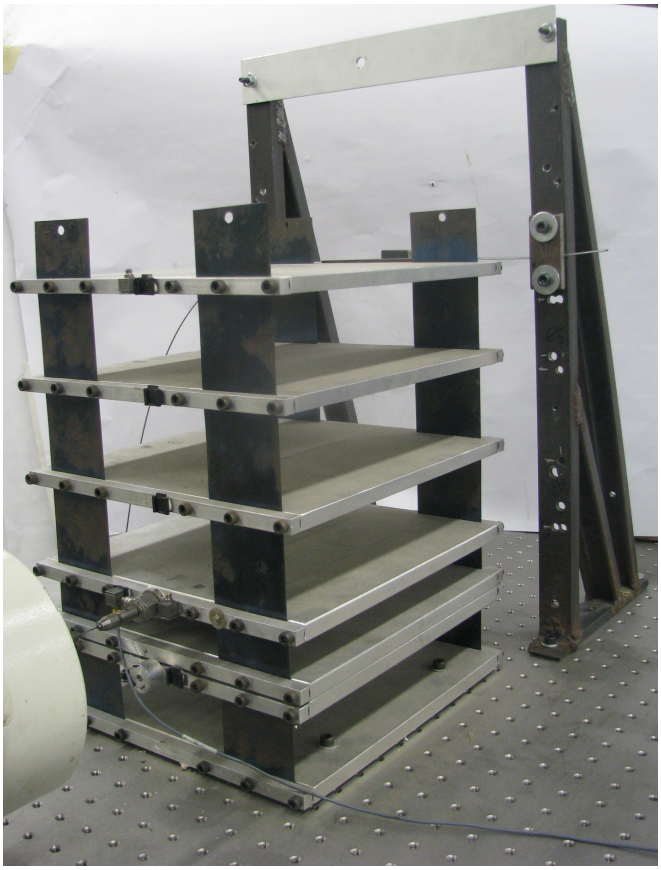

(b)

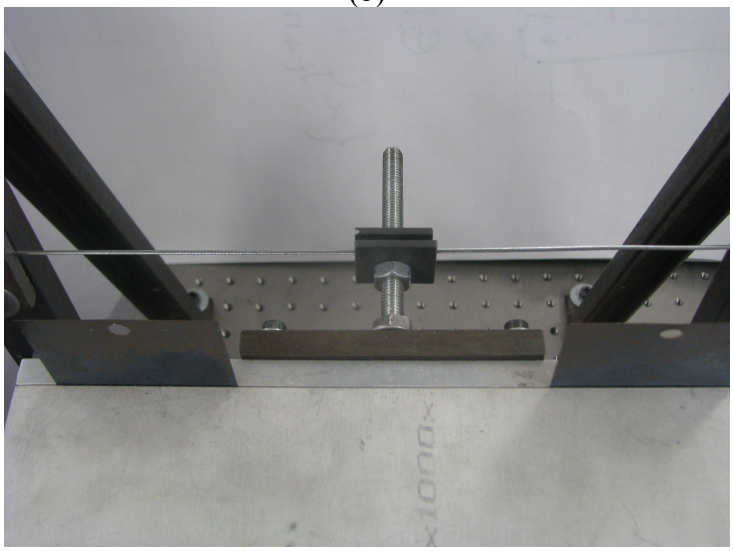

Figure 9: The experimental setup (a) and the string connected to the fifth floor (b).

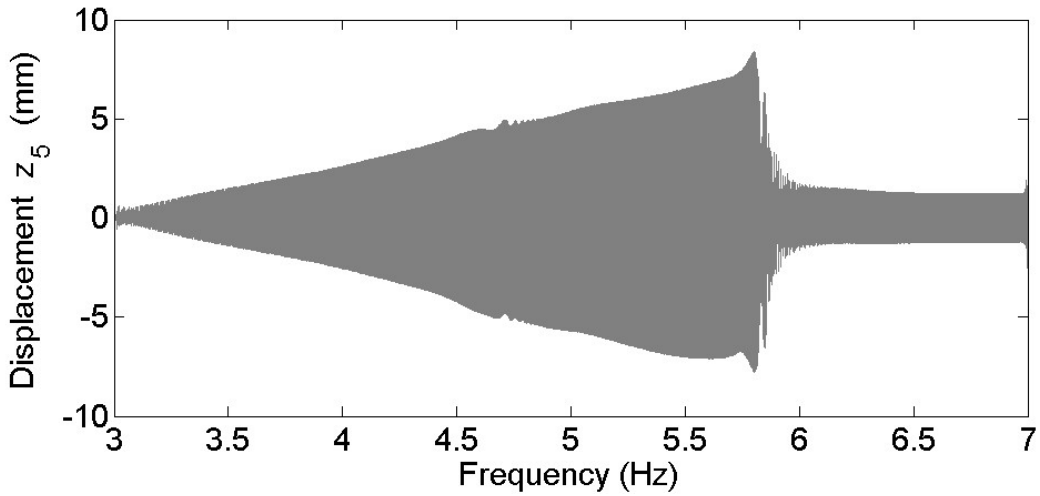

Figure 10: Response to a swept-sine force input.

5.1. Linear analysis

The stochastic subspace identification (SSI) [4] is adopted for a preliminary linear analysis, i.e., $p = 0$ in Eq. (1) and $u = f(t)$. The chosen time histories for the linear analysis correspond to the lowest excitation level (0.76 N_{rms}), because in this case the dynamic behaviour of the building may be considered linear, as also demonstrated by an approximately unitary coherence between input and outputs.

Modal parameters extracted by means of the linear analysis are summarised in Table 3 for the five modes, the experimental mode shapes are depicted in Fig. 11 and the classical stabilisation diagram is shown in Fig. 12.

Figure 13 shows the measured driving-point FRF of the system H_{22} with the fifth floor connected to the string and low excitation.

Table 3

Linear modal parameters of the building with string (low excitation)

Mode number	I	II	III	IV	V
Frequency (Hz)	2.94	6.13	10.23	14.61	27.58
Damping (%)	1.1	0.4	0.2	0.2	0.4

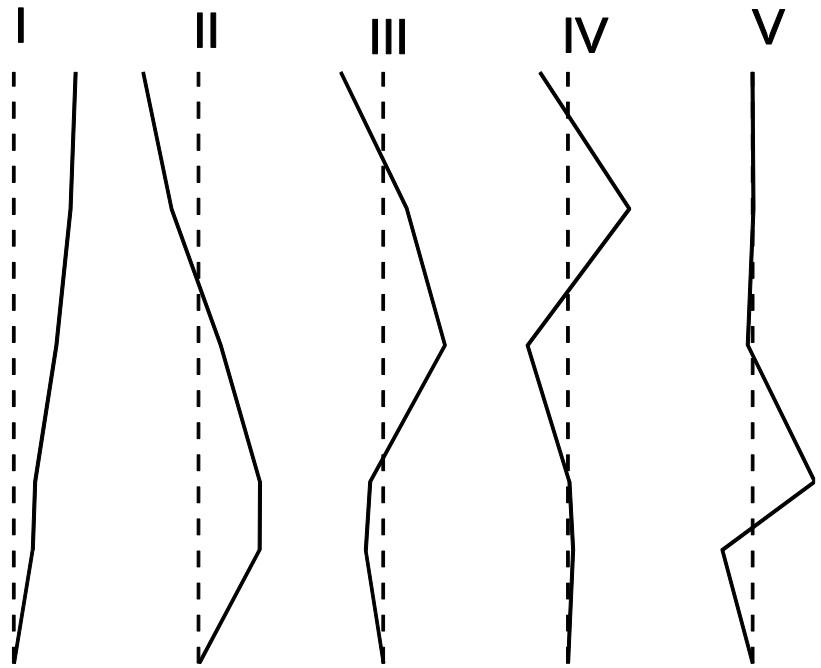

Figure 11: Linear mode shapes of the building with string (low excitation).

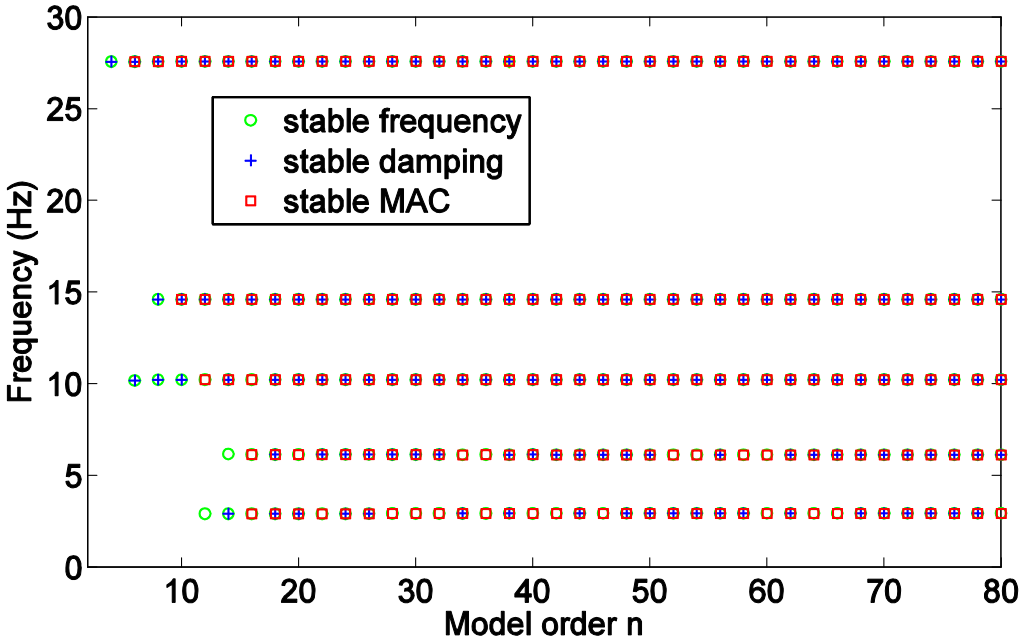

Figure 12: Stabilisation diagram computed by SSI for the system with string and low excitation level (0.76 N_{rms}). Stabilisation thresholds for natural frequency, damping ratio and MAC are 0.5 %, 5 % and 0.98, respectively.

Estimated FRFs are synthesised by summing contributions of the five modes with model orders spanning from 20 to 80: the mean and the standard deviation computed over these model orders are also shown in the figure, together with the residue, to give information about the difference between the measured and modelled FRFs. Small differences are only detectable next to the antiresonances, where the SNR is low.

In Fig. 14a the eigenfrequencies extracted with increasing model orders (from 2 to 200), are depicted and the modal mass is computed by imposing the largest scaled modal coefficient equal to unity. Table 2 indicates that a first estimate of the total mass is less than 12.5 kg and actually all physical poles are below this threshold, while the modal masses associated with spurious poles are generally larger. The histogram of the frequency occurrences (Fig. 14b) also indicates that physical poles are very stable, while spurious solutions do not stabilise as the model order increases and only give some

"noise" in the stabilisation diagram. These spurious modes appear at different frequencies, depending on the input

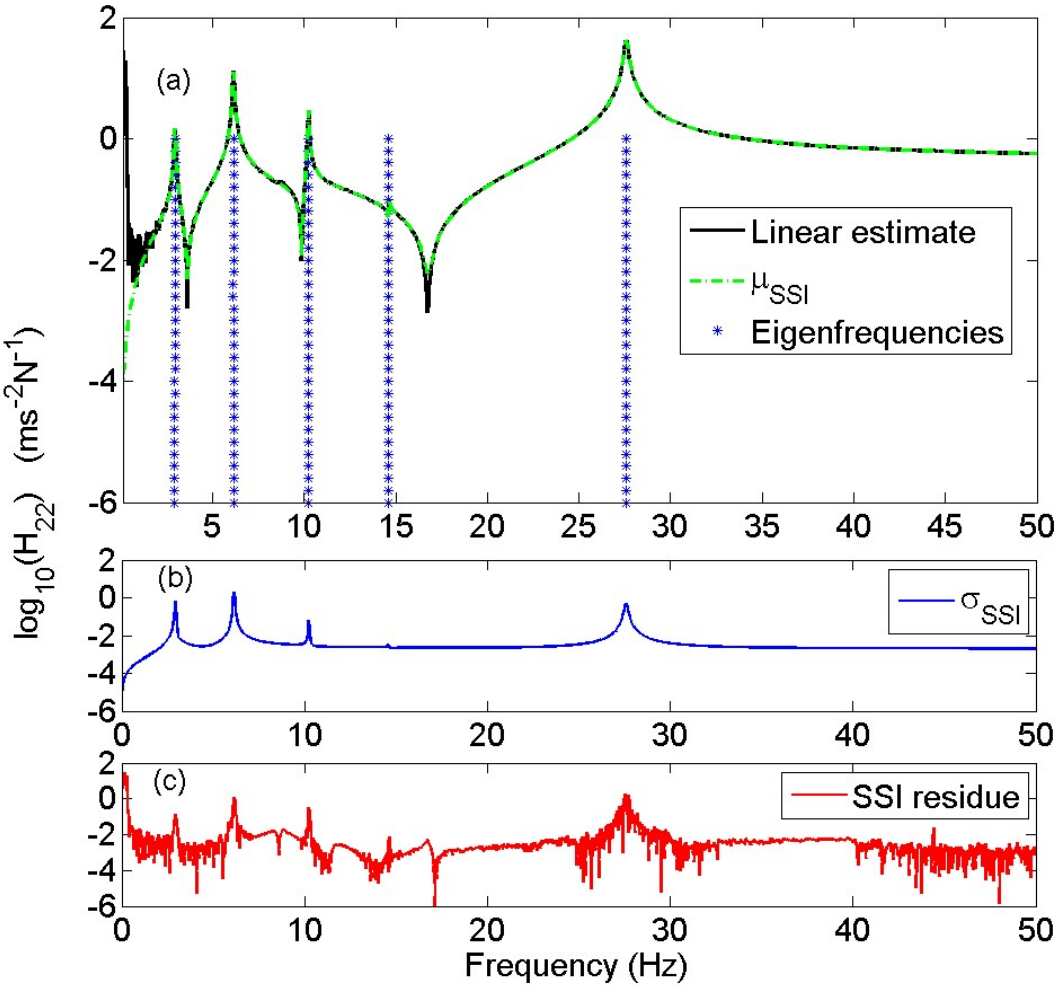

Figure 13: Driving-point FRF of the system with string and low excitation level (0.76 N_{rms}). Curve calculated using a linear estimator (mean between H_1 and H_2), solid line (a). Five-modes synthesis computed by SSI: eigenfrequencies with (even) model orders from 20 to 80 (asterisks, from bottom to top of the figure (a)), mean (dash dotted line (a)) and standard deviation (b) computed over these model orders; residue (c).

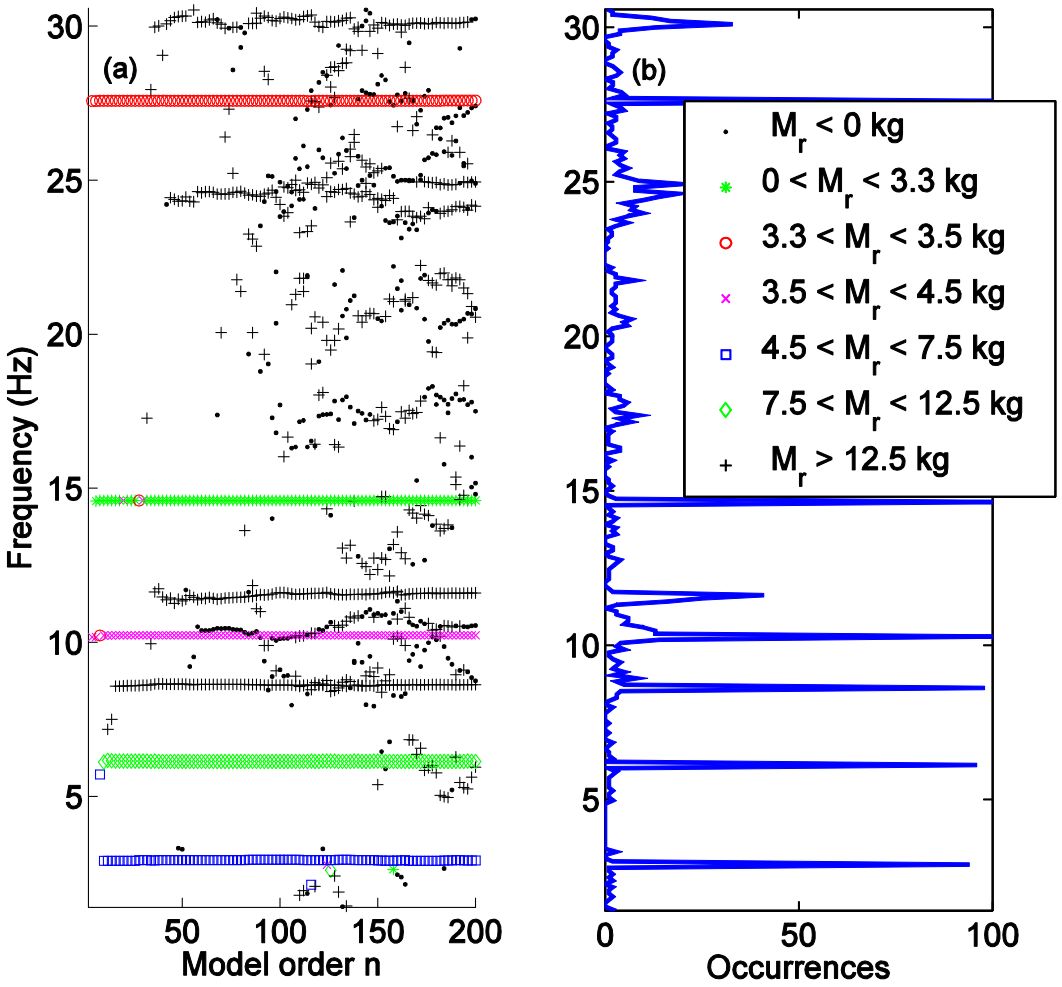

Figure 14: System with string and low excitation level (0.76 N_{rms}): eigenfrequencies extracted by SSI with increasing model orders (a); histogram of the frequency occurrences (b). The modal mass associated to each pole is indicated by different markers.

signal and on the noise level. It is interesting to note that two stable poles are identified around 8 Hz and 12 Hz, respectively. They correspond to modes of the heavy optical table supporting the building and indeed their modal masses are higher than the building total mass. No particular advantage is gained from their inclusion in the model.

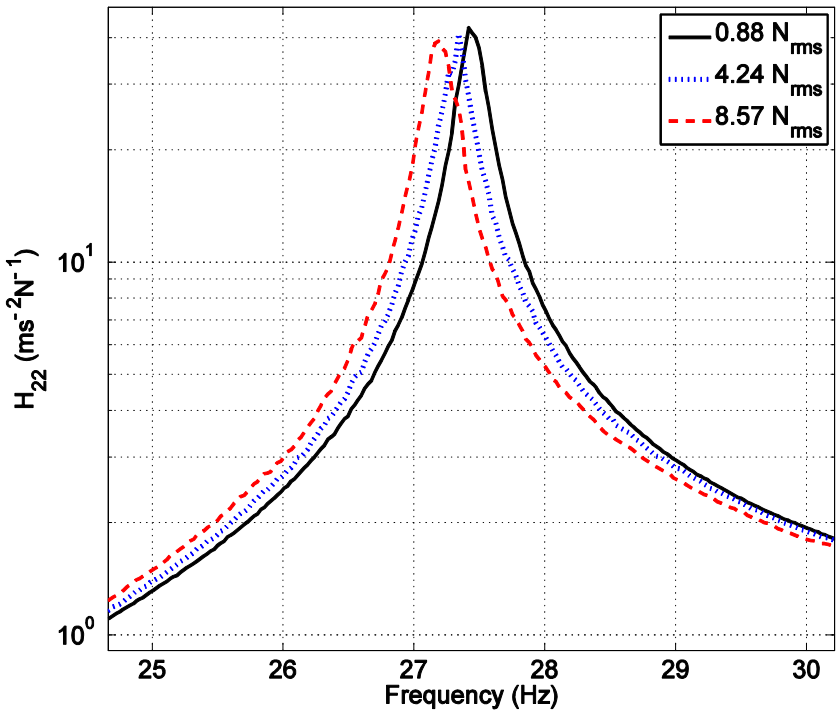

Figure 15: Magnification around the fifth mode of the driving-point FRF estimate with increasing force level, no string is connected.

5.2. Nonlinear analysis

A preliminary analysis conducted without the string showed that the fifth mode is affected by nonlinearity, which cannot be considered negligible. As shown in Fig. 15, by increasing the excitation level the fifth resonance peak moves to the left, while the other four peaks remain almost constant. This phenomenon would need a further study: it is probably due to the prominent relative displacement between the first and the second floor in the fifth mode (see Fig. 11), which is high in comparison with the length of the columns between the same floors of the building (the shortest ones, see Table 2). Each column is also subject to a compressive load due to the weight of the floors and moreover the columns between first and second floor were found not to be perfectly vertical at rest. The same behaviour is found after the string is mounted: the string has not a great influence on the resonance peak, because the fifth floor is next to a node of

the fifth mode (see Fig. 11).

Before performing the NSI analysis, the conventional linear FRF estimators H_1 and H_2 are computed, with parameters defined in Table 4 both for the linear and nonlinear case, to show distortions induced by nonlinearity. Figures from 16 to 19 show that these estimators give highly contaminated results in presence of nonlinearities and the extraction of underlying linear system properties is thus difficult or even impossible: in particular, there are considerable peak shifts and reduced amplitudes, harmonics appear and most of the antiresonances are masked as an effect of such nonlinear distortions.

Table 4

Signal processing parameters for H_1 and H_2 estimates

Δt (ms)	Blocksize	Averages	Nyquist frequency (Hz)	Percent overlap	Window
2.44	2^{14}	35	204.8	81	Hann

The equation of motion of the 5 DOFs vibrating system with a single nonlinearity between the fifth mass and ground is:

$$\mathbf{M}\ddot{\mathbf{z}}(t)+\mathbf{C}_v\dot{\mathbf{z}}(t)+\mathbf{K}\mathbf{z}(t)+\mu_1\mathbf{L}_{n1}g_1(t)=\mathbf{f}(t) \tag{28}$$

where $\mu_1 = k_{nl}$, $g_1(t)=z_5^3$, $\mathbf{L}_{n1}=\begin{bmatrix}0 & 0 & 0 & 0 & 1\end{bmatrix}^T$ and $\mathbf{f}=\begin{bmatrix}0 & f_2 & 0 & 0 & 0\end{bmatrix}^T$

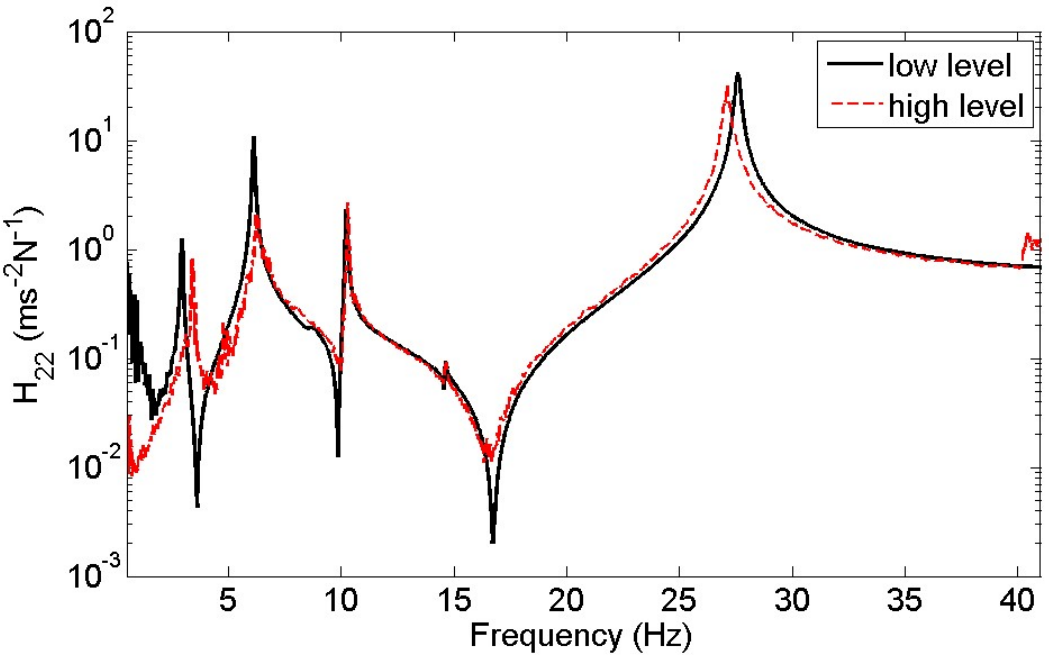

Figure 16: Comparison between linear estimates of H_{22} (mean between H_1 and H_2) of the building with string at low (0.76 N_{rms}, solid line) and high (20.95 N_{rms}, dotted line) excitation level.

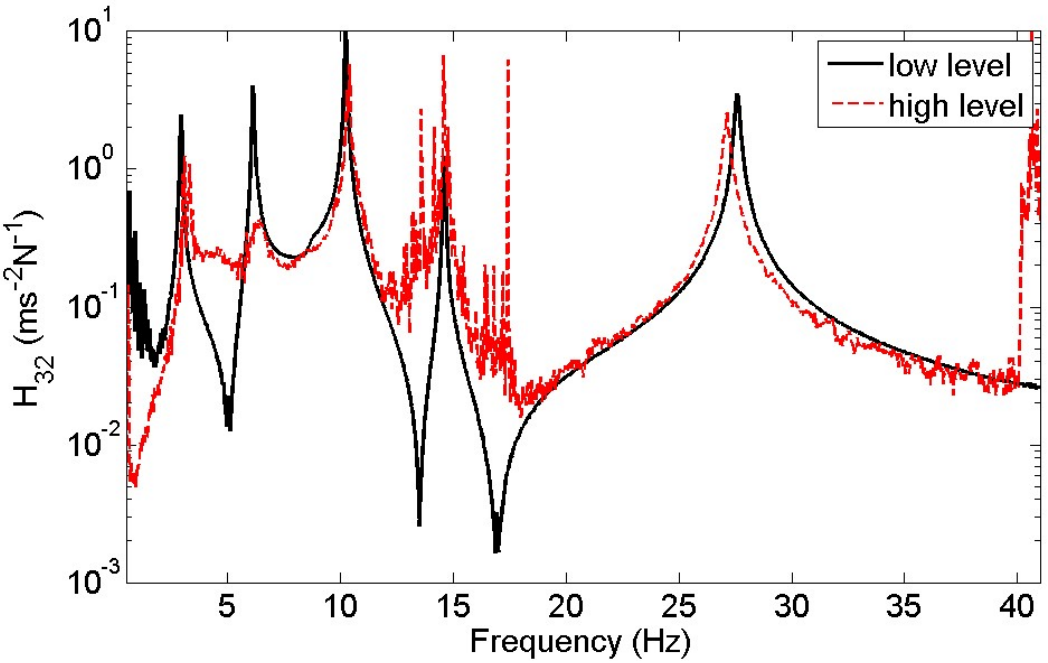

Figure 17: Comparison between linear estimates of H_{32} (mean between H_1 and H_2) of the building with string at low (0.76 N_{rms}, solid line) and high (20.95 N_{rms}, dotted line) excitation level.

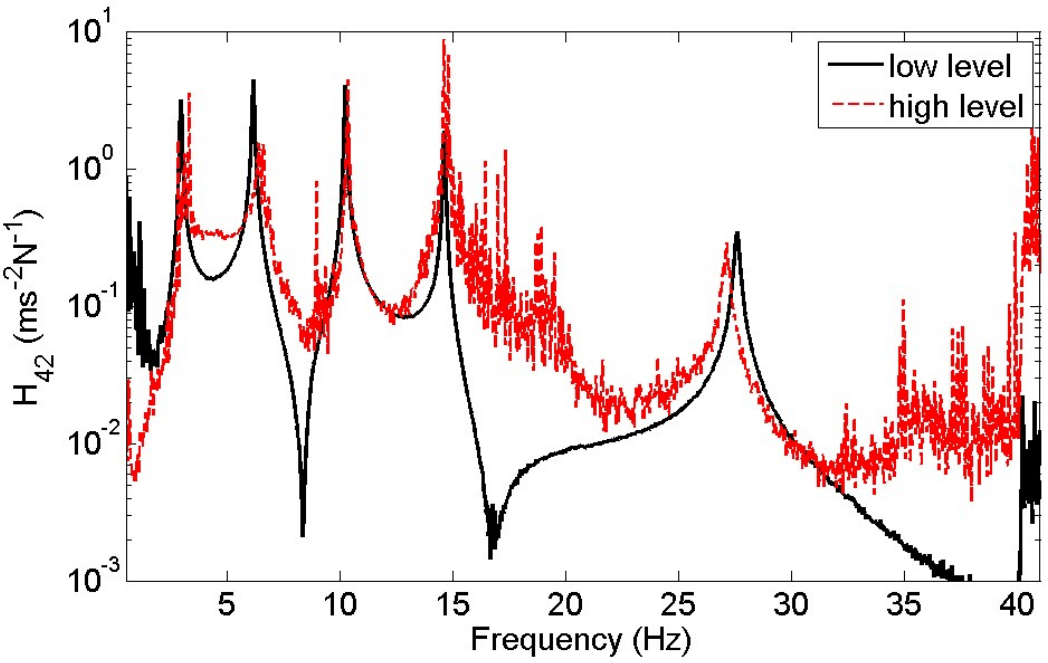

Figure 18: Comparison between linear estimates of H_{42} (mean between H_1 and H_2) of the building with string at low (0.76 N_{rms}, solid line) and high (20.95 N_{rms}, dotted line) excitation level.

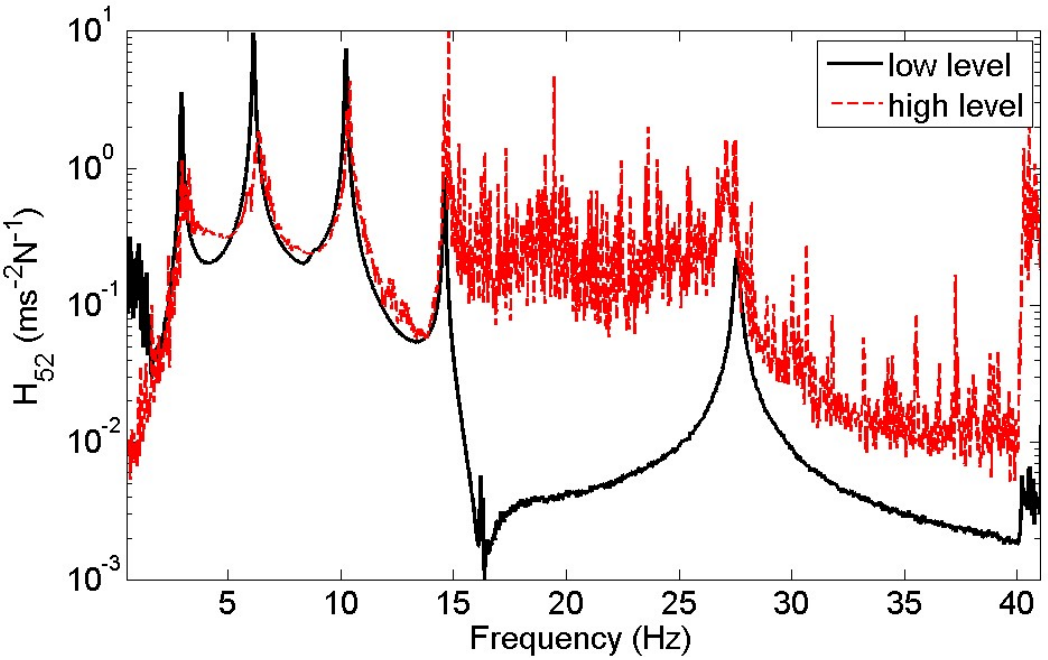

Figure 19: Comparison between linear estimates of H_{52} (mean between H_1 and H_2) of the building with string at low (0.76 N_{rms}, solid line) and high (20.95 N_{rms}, dotted line) excitation level.

The first column of the extended FRF matrix, Eq. (10), is built by the second column of the underlying linear system FRF matrix, because the force is applied at the second

floor only:

$$\mathbf{H}_{E1} = \begin{bmatrix} H_{12} & H_{22} & H_{32} & H_{42} & H_{52} \end{bmatrix}^T \tag{29}$$

Moreover, the reciprocity relationship $H_{pq} = H_{qp}$, which holds true since **H** is related to a linear system, can be applied and this allows computing $\mu_1 = k_{nl}$ from the second element of the following vector:

$$\mathbf{H}_{E2} = \begin{bmatrix} H_{E12} \\ H_{E22} \\ H_{E32} \\ H_{E42} \\ H_{E52} \end{bmatrix} = \mathbf{H}\mu_1\mathbf{L}_{n1} = k_{nl} \begin{bmatrix} ? & H_{12} & ? & ? & ? \\ H_{12} & H_{22} & H_{32} & H_{42} & H_{52} \\ ? & H_{32} & ? & ? & ? \\ ? & H_{42} & ? & ? & ? \\ ? & H_{52} & ? & ? & ? \end{bmatrix} \begin{Bmatrix} 0 \\ 0 \\ 0 \\ 0 \\ 1 \end{Bmatrix} = k_{nl} \begin{Bmatrix} ? \\ H_{52} \\ ? \\ ? \\ ? \end{Bmatrix} \tag{30}$$

The estimate of the nonlinear term coefficient is given by:

$$k_{nl} = \frac{H_{E22}(\omega)}{H_{E51}(\omega)} = \frac{H_{E22}(\omega)}{H_{52}(\omega)} = \frac{\sum_{r=1}^{n/2} num_r(\omega)}{\sum_{r=1}^{n/2} den_r(\omega)} \tag{31}$$

The eigenfrequencies of the underlying linear system extracted by NSI with increasing model orders (from 2 to 200, even values only) are shown in Fig. 20 together with the associated modal masses. By comparing this figure with Fig. 14, an increased number of spurious poles is evident, but their modal masses are usually negative or higher than those of physical poles (differences are often of several orders of magnitude). For this reason, and also exploiting classical stabilisation diagrams, they can be easily removed, making the identification task less difficult.

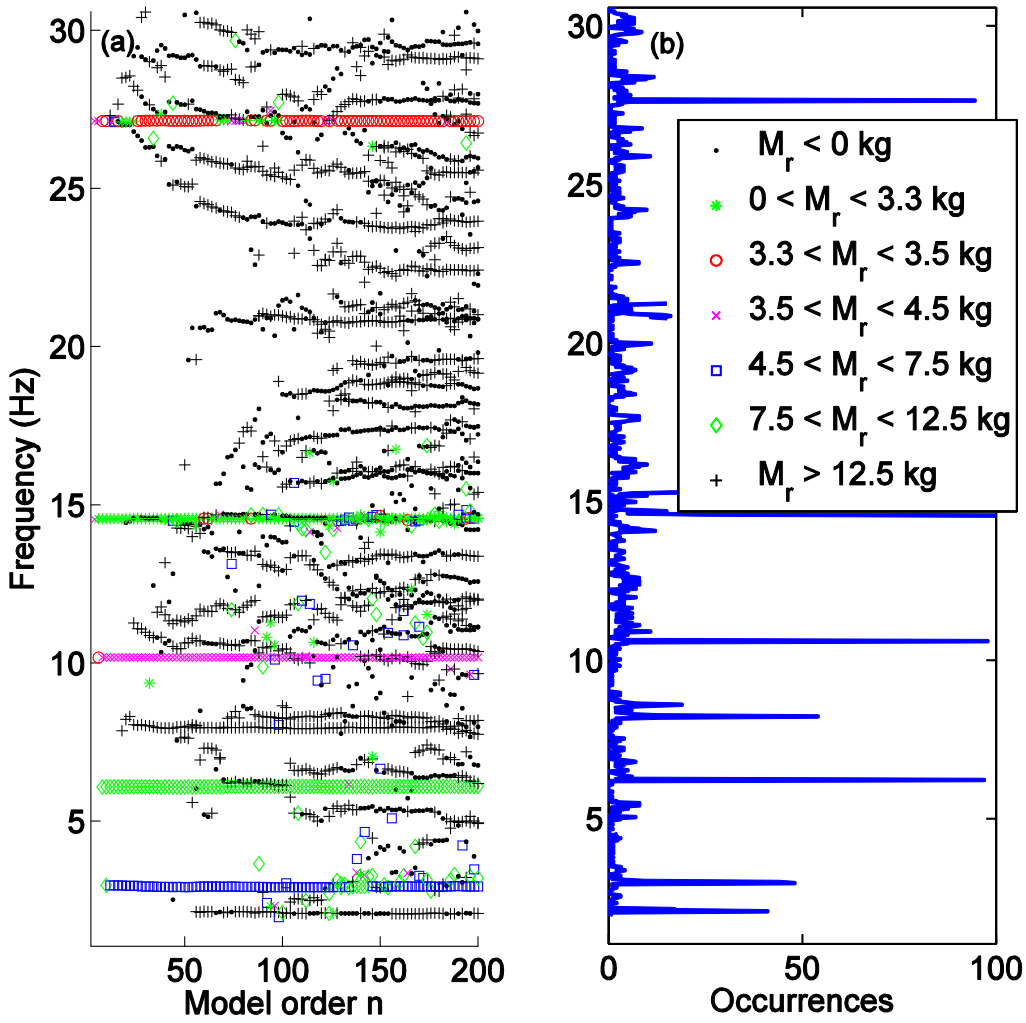

Figure 20: System with string and high excitation level (20.95 N_{rms}): eigenfrequencies of the underlying linear system extracted by NSI with increasing model orders (a); histogram of the frequency occurrences (b). The modal mass associated to each pole is indicated by different markers.

For example, a spurious pole around 2 Hz is visible, which corresponds to the low frequency of the filter used to obtain the fifth floor displacement from the acceleration: the corresponding modal mass is negative or very high (the damping is also negative). From the stabilisation diagram in Fig. 21 five stable modes are identified and the underlying linear system FRFs are synthesised using modal decomposition (Eq. 19).

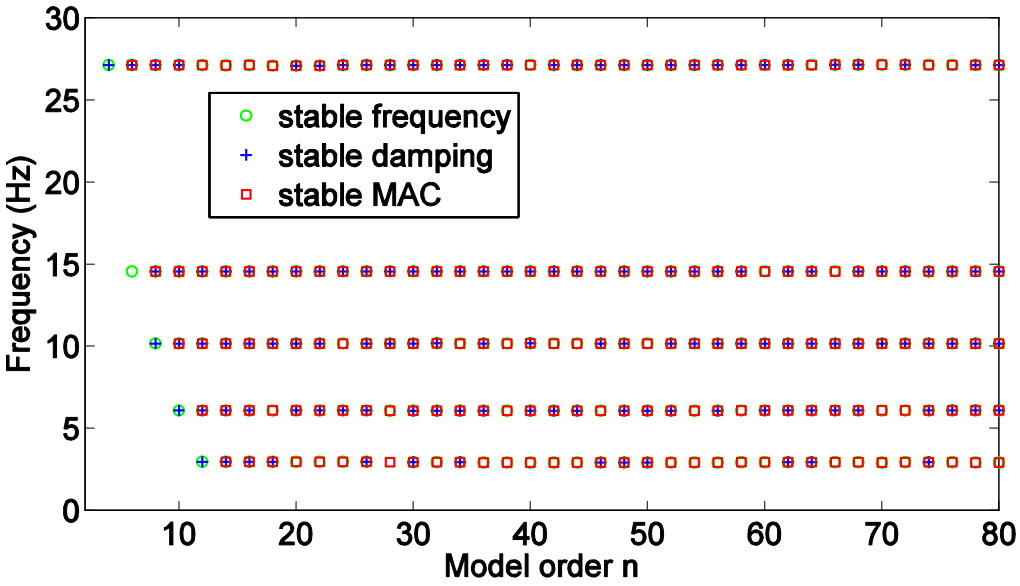

Figure 21: Stabilisation diagram computed by NSI for the system with string and high excitation level (20.95 N_{rms}). Stabilisation thresholds for natural frequency, damping ratio and MAC are 0.5 %, 5 % and 0.98, respectively.

Results concerning the driving-point FRF are depicted in Fig. 22 with model orders spanning from 30 to 60: the mean and the standard deviation computed over these model orders are also shown in the figure, together with the residue, to give information about the difference between the measured and modelled FRFs. The driving-point FRF shown in Fig. 22 is in good agreement with the low level excitation result and is quite insensitive to the model order, provided it is high enough.

Table 5 shows the relative errors in natural frequency and damping ratio between the low- and high-level models, together with the MAC between their mode shapes. Slight frequency shifts for the first four modes are found, while the fifth mode is affected by a higher frequency shift for the resonance peak: this is not surprising, since this mode showed

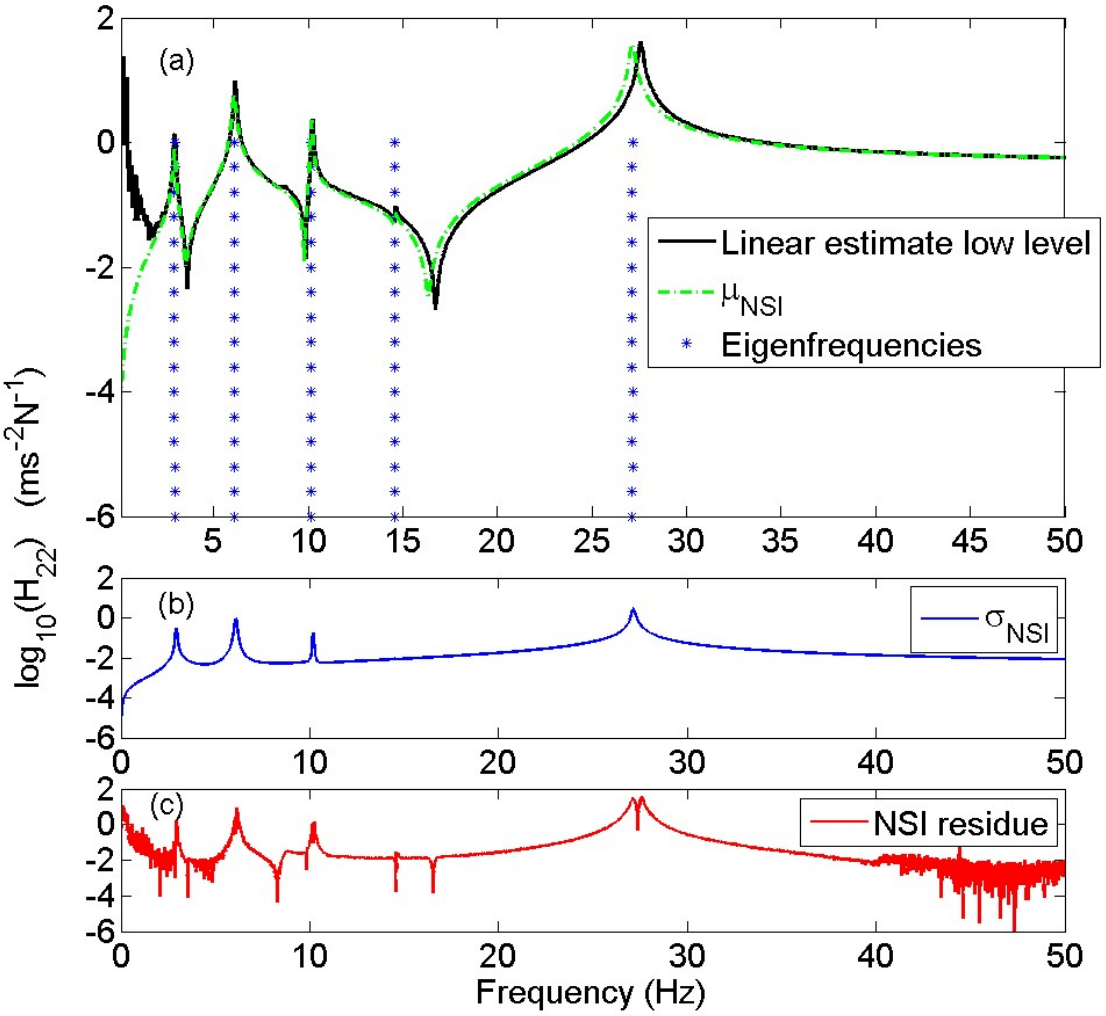

Figure 22: Driving-point FRF of the system with string. Curve calculated using a linear estimator for the low level excitation (0.76 N_{rms}), solid line (a). Five-modes synthesis computed by applying NSI to the high level excitation case (20.95 N_{rms}): eigenfrequencies with (even) model orders from 30 to 60 (asterisks, from bottom to top of the figure (a)), mean (dash dotted line (a)) and standard deviation (b) computed over these model orders; residue (c).

a nonlinear behaviour also without the string (see Fig. 15) and it is clear that this nonlinearity cannot be captured by the function $g_1(t) = z_5^3$ alone. Larger errors in the damping estimation are found, as reported by previous studies [13].

Table 5

Relative errors (NSI in the high level case *vs.* SSI in the low level case of Table 3) on

the estimated linear natural frequencies and damping ratios (in %) and diagonal MAC values

Mode	Error on f (%)	Error on ζ (%)	MAC
1	-0.58	-7.19	1.00
2	-0.75	91.12	1.00
3	-0.56	40.38	1.00
4	-0.34	53.20	1.00
5	-1.63	-6.30	1.00

The stabilisation diagram (Fig. 21) indicates that the lowest model order giving stable poles is $n = 26$ and this could be a reasonable choice. The poles corresponding to this model order give, by using Eq. (31), the coefficient of the cubic nonlinearity, as plotted in Fig. 23a. Unfortunately, none of the requirements for a successful identification is met: the imaginary part is not smaller than the corresponding real part and the frequency dependence of the coefficient isn't limited. However, a magnification of this figure between 2 and 15 Hz (Figure 24) indicates that the frequency variation is less pronounced in that frequency range, where the prominent contribution is given by the four physical (and well-identified) modes. A spectral mean in that range could then be a reasonable choice, and this was actually done in several numerical and experimental applications [1, 2, 3, 11, 13, 14, 17]. In the present case the spectral mean between 2 and 15 Hz is $k_{nl} = 5.84 \cdot 10^7 - i1.09 \cdot 10^7$ N/m^3, which could be considered as a first estimate.

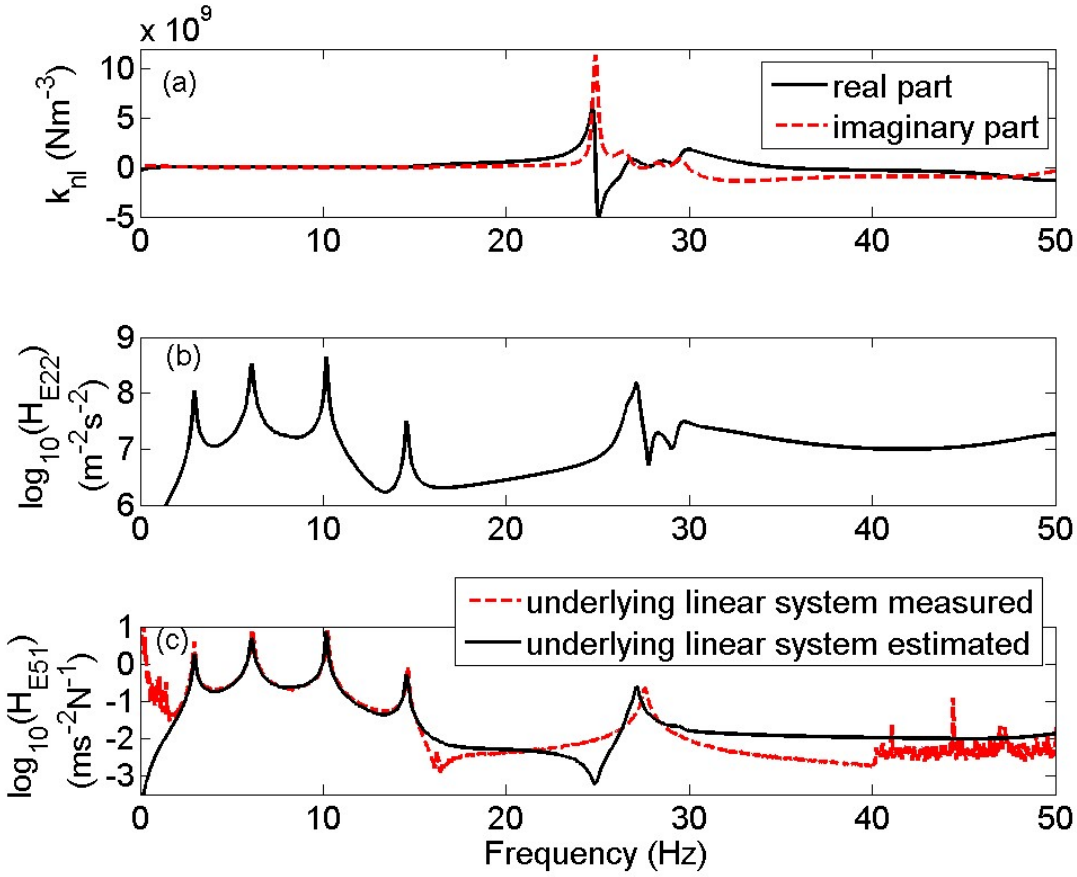

Figure 23: Coefficient of the cubic nonlinearity for the system with string and high excitation, model order n = 26 and all poles included. Real and imaginary part of the ratio (a), numerator (b), denominator (c).

However, it is interesting to explain the reason of the frequency dependence and complex-valuedness, which in most cases don't have any physical meaning. To better understand the origins of this behaviour, both numerator and denominator of the Eq. (31) are represented in Fig. 23b and in Fig. 23c, respectively. Both real and imaginary parts of coefficient k_{nl} show anomalous peaks around 25 Hz, which are due to an error in the antiresonance

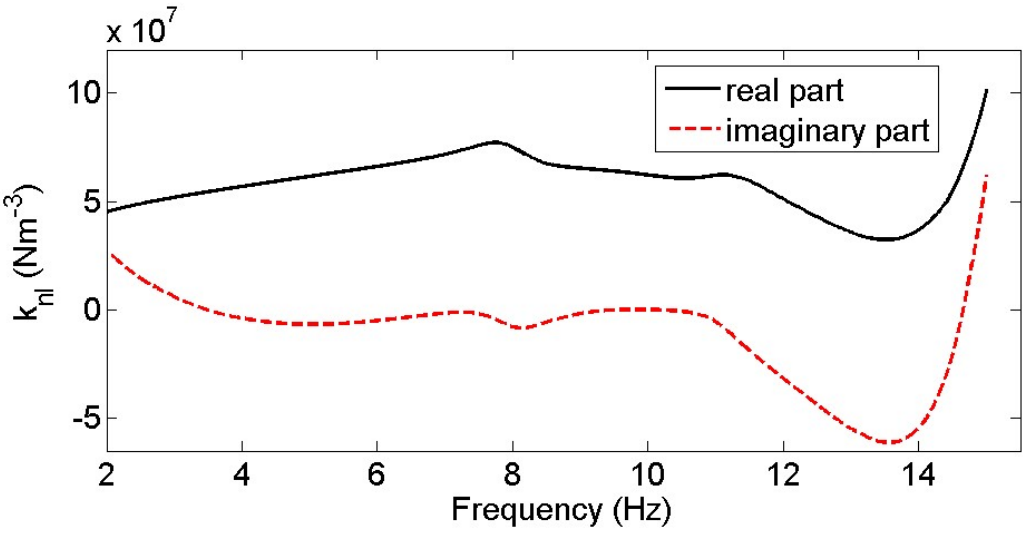

Figure 24: Real and imaginary parts of the coefficient k_{nl} computed by the contribution of all poles with model order n = 26 (magnification of figure 23a).

frequency, that should be around 16 Hz (recall that the denominator is H_{52} of the underlying linear system, see Fig. 23c). Note that, by increasing the model order, this specific error becomes smaller (the antiresonance moves to the left), but additional spurious poles appear. Moreover, in Fig. 23a some anomalous peaks are evident around 30 Hz, which seem to be caused by corresponding peaks in the numerator (the ratio would be constant if the numerator had the same form as the denominator). A deeper analysis is conducted to highlight the impact of the extracted poles on coefficient k_{nl}. By means of the tools proposed in this paper, the contribution of each pair of complex conjugate poles can be identified separately. Figure 25 shows the thirteen modal contributions to numerator (a) and denominator (b): spurious poles do not affect the denominator considerably (i.e., the underlying linear system FRF), their contributions being some orders of magnitude less than those of physical poles.

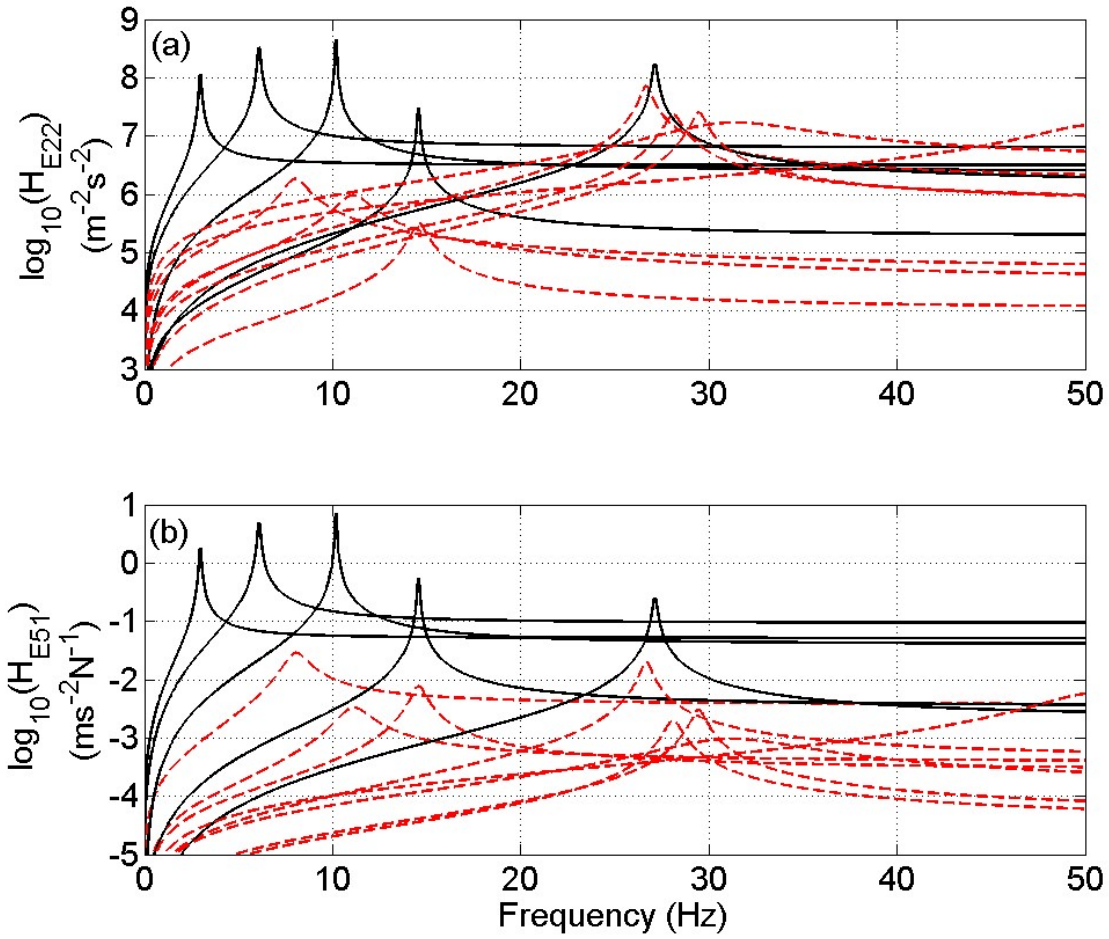

Figure 25: Modal contributions to the numerator (a) and denominator (b) of the cubic nonlinearity for the experimental system with string and high excitation (20.95 N_{rms}), model order n =26. Physical poles (solid line), spurious poles (dashed line).

On the contrary, contributions of spurious poles may be not negligible for the numerator (around 30 Hz in this case) and their removal is necessary. This task can be alleviated by computing the modal mass associated with each pole, as summarized in Table 6: most of the spurious poles can be removed by simply comparing their modal masses with the threshold value of 12.5 kg or even checking the sign.

Table 6

Underlying linear system modal parameters extracted by NSI for the system with string,

high excitation and model order $n = 26$

Pole number r	Physical (Ph) or spurious (Sp)	Frequency f_r (Hz)	Damping ratio ζ_r (%)	Modal mass M_r (kg)	$\rho = \frac{real(M_r)}{imag(M_r)}$
1	Ph	2.96	1.43	6.74	3.53
2	Ph	6.09	0.96	9.23	93.05
3	Sp	8.03	6.93	129.32	2.26
4	Ph	10.17	0.28	3.83	113.23
5	Sp	11.08	6.99	264.61	17.06
6	Ph	14.56	0.31	3.24	325.06
7	Sp	14.57	2.42	1.48	0.02
8	Sp	26.66	1.06	-76.62	4.89
9	Ph	27.13	0.38	3.32	78.22
10	Sp	28.10	1.42	215.05	0.96
11	Sp	29.45	1.17	-1127.97	2.06
12	Sp	31.13	11.25	-288.21	1.33
13	Sp	50.70	5.63	-152.29	1.75

If no information about the total mass is available, a stabilisation diagram of the modal masses can be used to remove spurious poles. In that case the modal mass can be adopted as extra stabilisation criterion in addition to the classical ones (frequency, damping and MAC). Note that even pole number 7 in Table 6 could be removed, although its frequency only differs from the previous one by 0.07%: in fact the last column of Table 6 indicates that the imaginary part of the seventh pole modal mass is

four orders of magnitude larger than that of the sixth pole, this helping in the removal of the former.

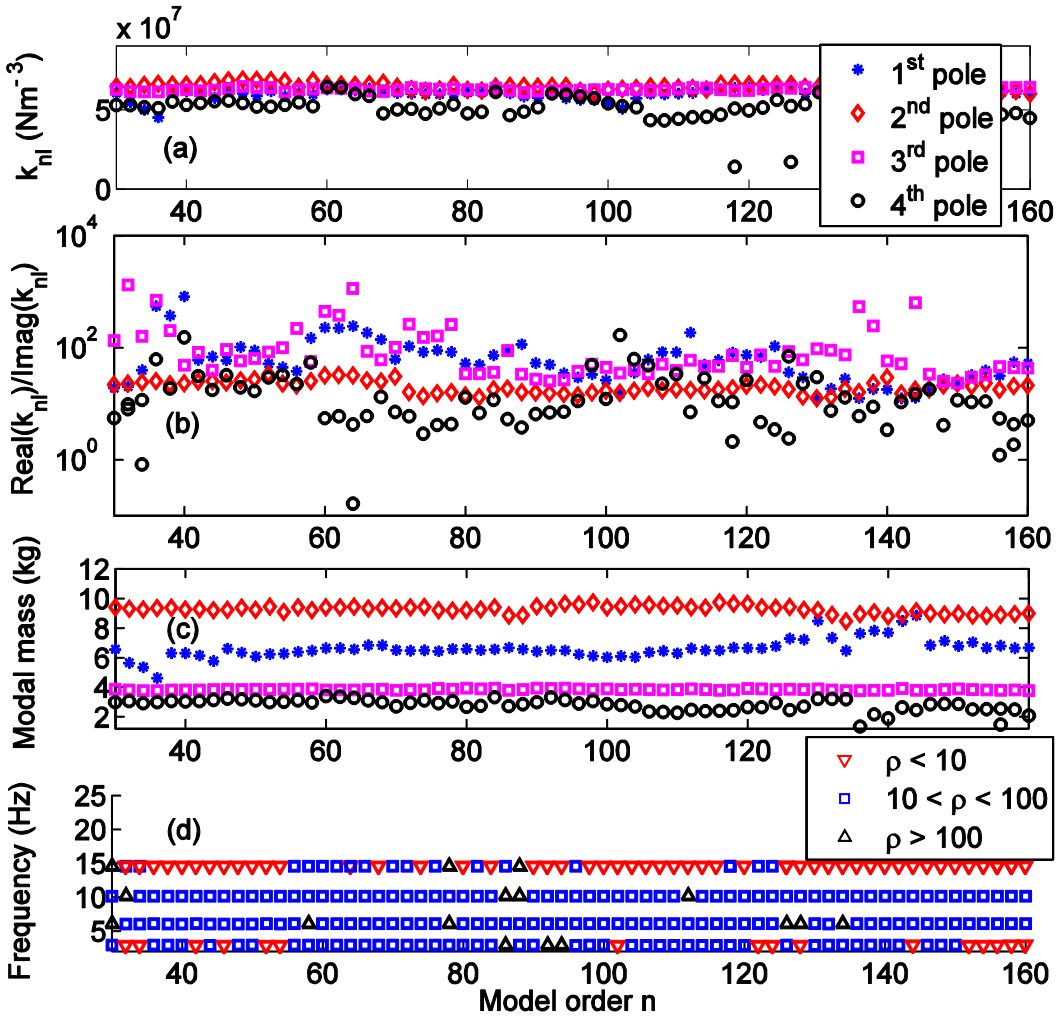

Figure 26: Stabilisation diagrams computed by NSI for the system with string and high excitation level. (a) real part; (b) ratio between the real and the imaginary parts of the spectral mean for the single-mode coefficient k_{nl}^r; (c) modal masses of the four physical poles (each pole is indicated by a different marker); (d) ratio ρ between the real and the imaginary parts of the modal mass associated to each pole.

In order to remove spurious poles, some user interaction is needed (thresholds should be defined for frequency and modal mass ranges) and clearly not all spurious poles can always be removed. It should be also mentioned that small errors, which are always existent in estimating the modal contributions from experimental data, induce some

frequency dependence in the coefficients of the nonlinear terms, even when all spurious poles have been removed. For this reason, the authors propose a new perspective: rather than assembling the nonlinear coefficient as the ratio of two sums, it can be estimated by a single physical mode only. In fact, numerical simulations (shown in Section 4) confirmed that if a certain mode is influenced by nonlinear effects, then this mode alone can be used to identify such nonlinearity.

To show how the identification procedure benefits by this approach, the spectral mean in the range between 2 and 40 Hz is computed for the coefficient of the cubic nonlinearity as it is "seen" by the first four modes, as follows:

$$k_{nl}^{r}(\omega) = \frac{num_r(\omega)}{den_r(\omega)}, \quad r = 1, 2, 3, 4 \tag{32}$$

(the fifth mode is not included because the nonlinearity does not depend upon the presence of the string). As for the numerical example, more powerful stabilisation diagrams than the classical ones are proposed in Fig 26: Fig. 26a and Fig. 26b show the real part and the ratio between the real part and the imaginary part of the spectral mean for the single-mode coefficient k_{nl}^{r}; Fig. 26c and Fig. 26d show the modal mass M_r associated to each pole and the corresponding ratio $\rho = \frac{real(M_r)}{imag(M_r)}$. Also in the experimental case, as well as in the numerical example, these diagrams indicate that for some model orders results of NSI are not reliable, while this information is missing in classical stabilisation diagrams.

The real parts of these spectral means are depicted in Fig. 26a as functions of the model order. There is some variability in k_{nl}^{r}, which seems to be correlated to the variability of the corresponding modal mass (Fig. 26c): both quantities in fact are computed by using the same matrix **B** of the state space model identified by NSI.

A stable coefficient is found by computing the "modal contribution" of the third mode

(k_{nl}^3), which is depicted in Fig. 27 as a function of the frequency for the model order n = 30. It corresponds approximately to the mean value of the coefficient with n spanning from 30 to 160. The frequency dependence has practically vanished and the imaginary part is small (the real part of k_{nl}^3 is $6.28 \cdot 10^7$ N/m^3, the imaginary part is $-4.7 \cdot 10^5$ N/m^3).

In Table 7 the mean and standard deviation (with n spanning from 30 to 160) for the single-mode nonlinear coefficients are summarised: as also confirmed by Fig. 26a, the variability is minimum for the third mode and maximum for the fourth mode. In fact, estimates based on the fourth mode should not be considered reliable on the basis of the information contained in Fig. 26: in general, and in contrast to third mode, the fourth mode shows the highest imaginary part for both the nonlinear coefficient and the modal mass. This is an indication of identification problems, as also found in the numerical application (Fig. 5).

Finally, the comparison of Figures 27 and 23a reveals that substantial improvements can be obtained by NSI if spurious poles are removed and if well identified modes only are included in the estimation of nonlinear effects.

Table 7

Nonlinear coefficient estimates (model orders from 30 to 160, even values only)

Mode	k_{nl}^r (N/m^3)	
r	mean	*std*
1	$5.97 \cdot 10^7$	$3.39 \cdot 10^6$

2	$6.41 \cdot 10^7$	$2.59 \cdot 10^6$
3	$6.28 \cdot 10^7$	$9.81 \cdot 10^5$
4	$5.11 \cdot 10^7$	$1.06 \cdot 10^7$

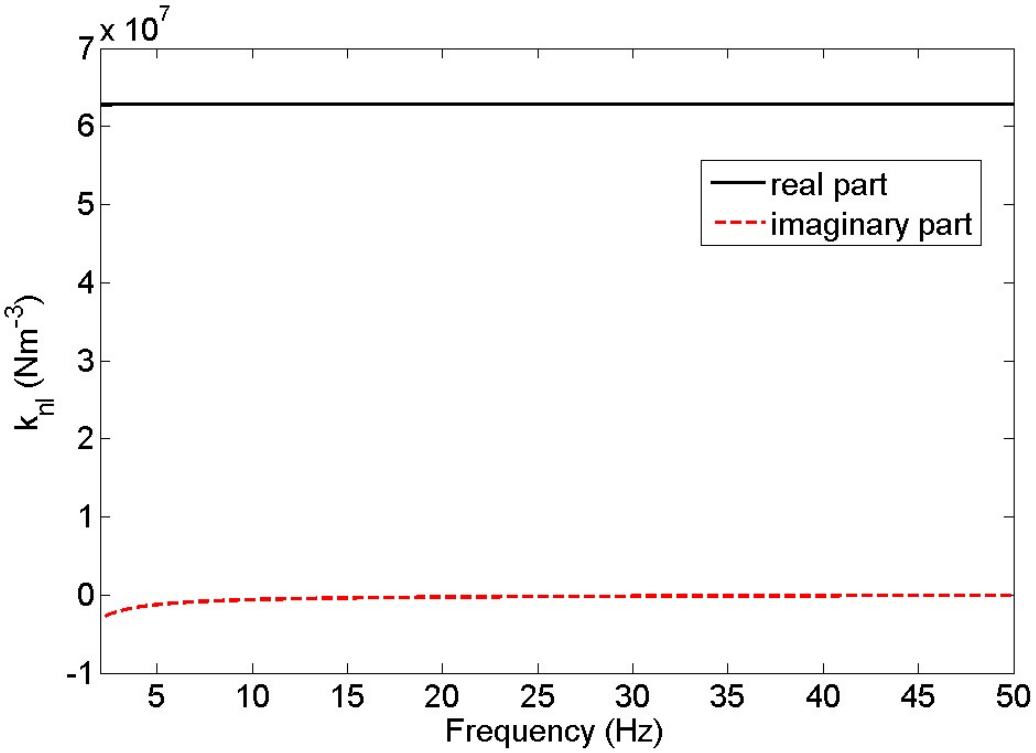

Figure 27: Real and imaginary parts of the coefficient k_{nl}^3 computed by the contribution of the third mode only (eigenfrequency around 10.17 Hz) with model order $n = 30$.

5.3. Softening nonlinearity affecting mode 5

The nonlinear analysis conducted so far illustrates a new decoupling strategy and introduces new tools to understand the contributions of the different poles. The last part of the study is concerned with the softening nonlinearity affecting the fifth mode. To this purpose, the model of Eq. (28) is modified as follows, to take into account the nonlinearity originating from the relative displacement between the first and the second

floor:

$$\mathbf{M}\ddot{\mathbf{z}}(t)+\mathbf{C}_v\dot{\mathbf{z}}(t)+\mathbf{K}\mathbf{z}(t)+\mu_1\mathbf{L}_{n1}g_1(t)+\mu_2\mathbf{L}_{n2}g_2(t)+\mu_3\mathbf{L}_{n3}g_3(t)=\mathbf{f}(t) \tag{33}$$

where $g_1(t)=z_5^3$, $\mathbf{L}_{n1}=\begin{bmatrix}0 & 0 & 0 & 0 & 1\end{bmatrix}^T$, $g_2(t)=(z_2-z_1)^2$, $g_3(t)=(z_2-z_1)^3$ and $\mathbf{L}_{n2}=\mathbf{L}_{n3}=\begin{bmatrix}-1 & 1 & 0 & 0 & 1\end{bmatrix}^T$.

Figure 28 shows the estimates computed by NSI as functions of the frequency. As expected, the coefficient μ_1 is again quite constant in the frequency range up to 15 Hz (likewise as depicted in Fig. 24); on the contrary, the coefficients μ_2 and μ_3 manifest a high variability in the same low frequency range, while they are quite constant after 15 Hz, where the fifth mode contribution is dominant.

Figure 29 shows the nonlinear contributions to the stiffness curves computed by NSI with n = 26: the spectral mean $\langle\mu_1\rangle=6.32\cdot10^7-\mathrm{i}1.68\cdot10^6\ \mathrm{N/m^3}$ is obtained between 2 and 15 Hz for the first coefficient; $\langle\mu_2\rangle=8.48\cdot10^5-\mathrm{i}1.16\cdot10^4\ \mathrm{N/m^2}$ and $\langle\mu_3\rangle=-1.77\cdot10^8+\mathrm{i}1.84\cdot10^7\ \mathrm{N/m^3}$ are obtained between 15 and 50 Hz for the second and third coefficient, respectively.

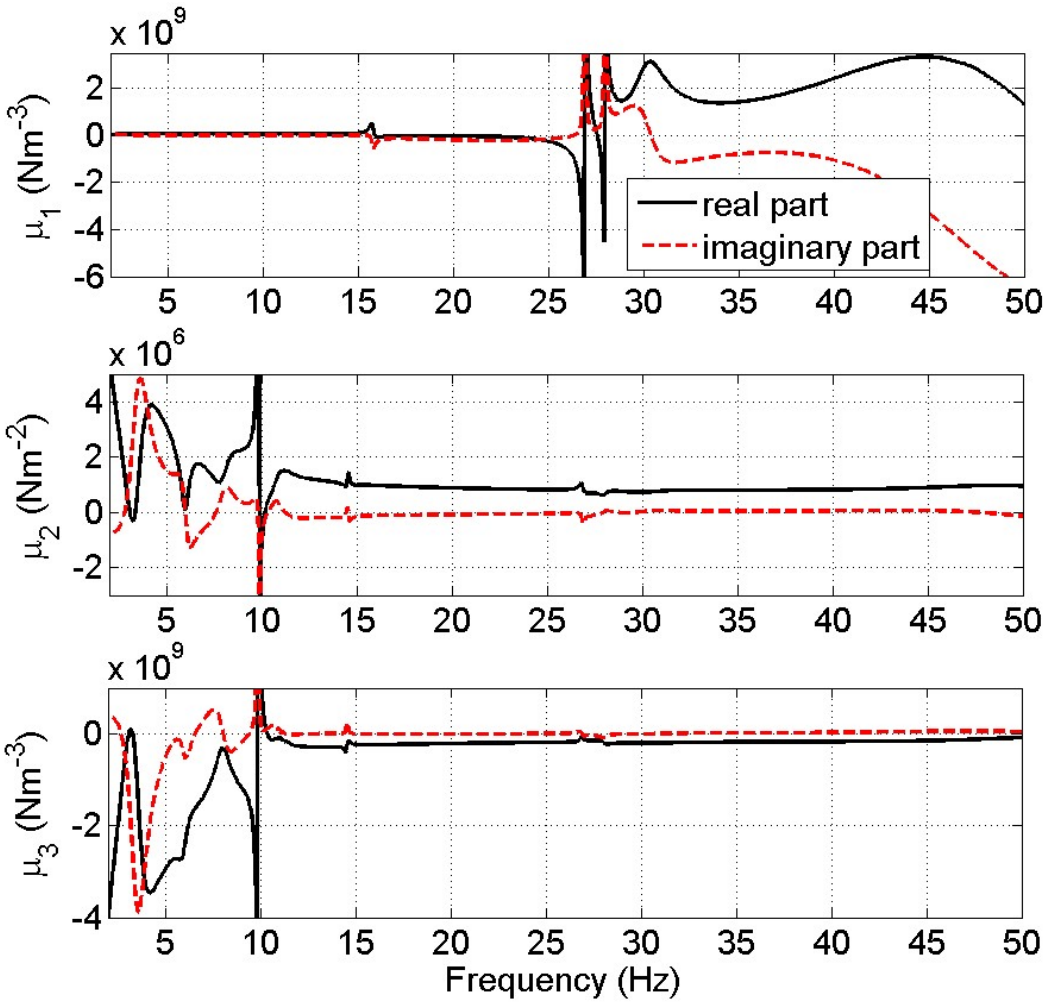

Figure 28: Real and imaginary parts of the coefficients μ_1, μ_2, μ_3 in Eq. 33, computed by NSI for the experimental system with string and high excitation (20.95 N_{rms}), model order n =26.

In particular, Fig. 29b indicates a non-symmetrical behaviour: a softening effect for negative relative displacements and a little hardening effect for positive relative displacements. However, it should be stressed that relative displacements were not directly measured but obtained by twice integrating the corresponding accelerations and then by filtering the resulting signal (between 2 and 160 Hz), to remove the spurious components introduced by the integration procedure. Consequently, the true mean value of the time histories cannot be obtained and a displacement sensor would be desirable to properly capture the nonlinearity, as usually done in presence of non-symmetrical

behaviour [14].

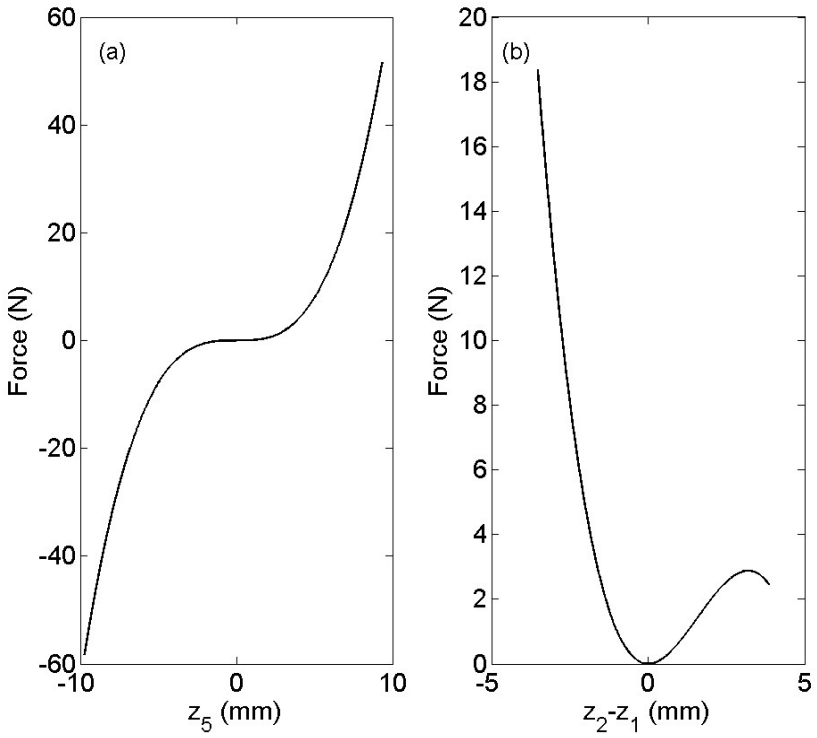

Figure 29: NSI estimates of the nonlinear contributions to the stiffness curves of the experimental system with string and high excitation (20.95 N_{rms}), model order n =26. Nonlinear contribution due to the string (a), nonlinear contribution originating from the relative displacement between the first and the second floor (b).

5. Conclusions

Aim of the present study is to introduce modal decoupling tools in the nonlinear subspace identification (NSI). This method provides a means of obtaining a set of parameters related to the underlying linear system in addition to nonlinear characteristics. Previous works on this subject reported the presence of artefacts in the parameter estimates of the nonlinear terms, which are returned in the form of frequency-

dependent and complex-valued coefficients.

In the paper it is shown that spurious modes, due to an over-estimation of the system order, may affect the estimates of the nonlinear coefficients and are among the factors which cause their frequency dependence and complex-valuedness. They should be removed once their contributions to the system dynamics have been identified. At the same time, the tools developed in the paper make it possible to identify and to assess modal contributions of physical poles on the nonlinear dynamics. This capability paves the way for a new perspective, which is adopted here for the experimental identification of a multi-degree-of-freedom system connected to a thin metallic wire.

Comparing Figures from 16 to 19 with Fig. 22 and Fig. 27 proves that the experimental case is challenging and the identification tool very effective: significant improvement of the estimates is achieved by NSI, which now incorporates most of the tools adopted by standard linear identification procedures.

References

[1] G. Kerschen, K. Worden, A.F. Vakakis, J.-C. Golinval, Past, present and future of nonlinear system identification in structural dynamics, Mechanical Systems and Signal Processing 20 (2006), pp. 505-592.

[2] S. Marchesiello, L. Garibaldi, A time domain approach for identifying nonlinear vibrating structures by subspace methods, Mechanical Systems and Signal Processing 22 (2008), pp. 81-101

[3] D.E. Adams, R.J. Allemang, A frequency domain method for estimating the parameters of a non-linear structural dynamic model through feedback, Mechanical Systems and Signal Processing 14 (2000), pp. 637-656.

[4] P. Van Overschee, B. De Moor, Subspace Identification for Linear Systems:

Theory-Implementation-Applications, Kluwer Academic Publishers, Dordrecht, The Netherlands, 1996.

[5] E. Gandino, L. Garibaldi, S. Marchesiello, Covariance-driven subspace identification: A complete input–output approach, Journal of Sound and Vibration 332 (2013), pp. 7000-7017.

[6] L. Mevel, A. Benveniste, M. Basseville, M. Goursat, B.Peeters, H. Van der Auweraer, A. Vecchio, Input/output versus output-only data processing for structural identification – Application to in-flight data analysis, Journal of Sound and Vibration 295(3-5) (2006), pp. 531-552.

[7] E. Reynders, G. De Roeck, Reference-based combined deterministic-stochastic subspace identification for experimental and operational modal analysis, Mechanical Systems and Signal Processing 22(3) (2008), pp. 617-637.

[8] E. Reynders, R. Pintelon, G. De Roeck, Uncertainty bounds on modal parameters obtained from stochastic subspace identification, Mechanical Systems and Signal Processing 22(4) (2008), pp. 948-969.

[9] Y. Zhang, Z. Zhang, X. Xu, H. Hua, Modal parameter identification using response data only, Journal of Sound and Vibration 282(1-2) (2005), pp. 367-380.

[10] F. Magalhaes, A. Cunha, E. Caetano, Online automatic identification of the modal parameters of a long span arch bridge, Mechanical Systems and Signal Processing 23(2) (2009), pp. 316-329.

[11] J.P. Noël, G. Kerschen, Frequency-domain subspace identification for nonlinear mechanical systems, Mechanical Systems and Signal Processing 40 (2013), pp. 701–717

[12] S. Vanlanduit, P. Verboven, P. Guillaume, J. Schoukens, An automatic

frequency domain modal parameter estimation algorithm, Journal of Sound and Vibration 265(3) (2003), pp. 647-661.

[13] J.P. Noël, S. Marchesiello, G. Kerschen, Subspace-based identification of a nonlinear spacecraft in the time and frequency domains, Mechanical Systems and Signal Processing 43 (2014), pp. 217–236

[14] S. Marchesiello, L. Garibaldi, Identification of clearance-type nonlinearities, Mechanical Systems and Signal Processing 22 (2008), pp. 1133–1145

[15] R. Allemang, Course Notes, http://www.sdrl.uc.edu/academic-course-info/vibrations-iii-20-263-663, 1999

[16] G. Gatti, M.J. Brennan, I. Kovacic, On the interaction of the responses at the resonance frequencies of a nonlinear two degrees-of-freedom system, Physica D, 239 (2010), pp. 591–599

[17] E. Gandino, S. Marchesiello, Identification of a Duffing Oscillator under Different Types of Excitation, Mathematical Problems in Engineering (2010), Volume 2010, Article ID 695025.

List of tables

List of figures

contribution of the *r*th mode only (model order $n = 22$).

Figure 8: Multi-storey building with nonlinearity produced by a thin wire.

Figure 9: The experimental setup (a) and the string connected to the fifth floor (b).

Figure 10: Response to a swept-sine force input.

Figure 11: Linear mode shapes of the building with string (low excitation).

Figure 12: Stabilisation diagram computed by SSI for the system with string and low excitation level (0.76 N_{rms}). Stabilisation thresholds for natural frequency, damping ratio and MAC are 0.5 %, 5 % and 0.98, respectively.

Figure 13: Driving-point FRF of the system with string and low excitation level (0.76 N_{rms}). Curve calculated using a linear estimator (mean between H_1 and H_2), solid line (a). Five-modes synthesis computed by SSI: eigenfrequencies with (even) model orders from 20 to 80 (asterisks, from bottom to top of the figure (a)), mean (dash dotted line (a)) and standard deviation (b) computed over these model orders; residue (c).

Figure 14: System with string and low excitation level (0.76 N_{rms}): eigenfrequencies extracted by SSI with increasing model orders (a); histogram of the frequency occurrences (b). The modal mass associated to each pole is indicated by different markers.

Figure 15: Magnification around the fifth mode of the driving-point FRF estimate with increasing force level, no string is connected.

Figure 16 Comparison between linear estimates of H_{22} (mean between H_1 and H_2) of the building with string at low (0.76 N_{rms}, solid line) and high (20.95 N_{rms}, dotted line) excitation level.

Figure 17: Comparison between linear estimates of H_{32} (mean between H_1 and H_2) of the building with string at low (0.76 N_{rms}, solid line) and high (20.95 N_{rms},

dotted line) excitation level.

Figure 18: Comparison between linear estimates of H_{42} (mean between H_1 and H_2) of the building with string at low (0.76 N_{rms}, solid line) and high (20.95 N_{rms}, dotted line) excitation level.

Figure 19: Comparison between linear estimates of H_{52} (mean between H_1 and H_2) of the building with string at low (0.76 N_{rms}, solid line) and high (20.95 N_{rms}, dotted line) excitation level.

Figure 20: System with string and high excitation level (20.95 N_{rms}): eigenfrequencies of the underlying linear system extracted by NSI with increasing model orders (a); histogram of the frequency occurrences (b). The modal mass associated to each pole is indicated by different markers.

Figure 21: Stabilisation diagram computed by NSI for the system with string and high excitation level (20.95 N_{rms}). Stabilisation thresholds for natural frequency, damping ratio and MAC are 0.5 %, 5 % and 0.98, respectively.

Figure 22: Driving-point FRF of the system with string. Curve calculated using a linear estimator for the low level excitation (0.76 N_{rms}), solid line (a). Five-modes synthesis computed by applying NSI to the high level excitation case (20.95 N_{rms}): eigenfrequencies with (even) model orders from 30 to 60 (asterisks, from bottom to top of the figure (a)), mean (dash dotted line (a)) and standard deviation (b) computed over these model orders; residue (c).

Figure 23: Coefficient of the cubic nonlinearity for the system with string and high excitation, model order n = 26 and all poles included. Real and imaginary part of the ratio (a), numerator (b), denominator (c).

Figure 24: Real and imaginary parts of the coefficient k_{nl} computed by the

contribution of all poles with model order n = 26 (magnification of figure 23a).

Figure 25: Modal contributions to the numerator (a) and denominator (b) of the cubic nonlinearity for the experimental system with string and high excitation (20.95 N_{rms}), model order n =26. Physical poles (solid line), spurious poles (dashed line).

Figure 26 Stabilisation diagrams computed by NSI for the system with string and high excitation level. (a) real part; (b) ratio between the real and the imaginary parts of the spectral mean for the single-mode coefficient k_{nl}^{r}; (c) modal masses of the four physical poles (each pole is indicated by a different marker); (d) ratio ρ between the real and the imaginary parts of the modal mass associated to each pole.

Figure 27: Real and imaginary parts of the coefficient k_{nl}^{3} computed by the contribution of the third mode only (eigenfrequency around 10.17 Hz) with model order n = 30.

Figure 28: Real and imaginary parts of the coefficients μ_1, μ_2, μ_3 in Eq. 33, computed by NSI for the experimental system with string and high excitation (20.95 N_{rms}), model order n =26.

Figure 29: NSI estimates of the nonlinear contributions to the stiffness curves of the experimental system with string and high excitation (20.95 N_{rms}), model order n =26. Nonlinear contribution due to the string (a), nonlinear contribution originating from the relative displacement between the first and the second floor (b).